MRI R2* captures inflammation in disconnected brain structures after stroke: a translational study

Ismail Koubiyr, Takayuki Yamamoto, Laurent Petit, Nadege Dubourdieu, Elena Avignone, Elise Cozensa, Chloe Galmiche, Hikaru Fukutomi, Igor Sibon, Vincent Dousset, et al.

MRI R2* captures inflammation in disconnected brain structures after stroke: a translational study

Ismail Koubiyr *[1,2], Takayuki Yamamoto *[3], Laurent Petit [4], Nadège Dubourdieu [1], Elena Avignone [1], Elise Cozensa [4], Chloé Galmiche [1], Hikaru Fukutomi [3], Igor Sibon [5], Vincent Dousset [1,6], Michel Thiebaut de Schotten [4,7], Aude Panatier [1], Marion Tible [§1], Thomas Tourdias [§†1,6]

* *These authors contributed equally to this work and are co-first authors*

[§] *These authors shared the supervision of this work and are co-last authors*

†Corresponding author

[1] Univ. Bordeaux, INSERM, Neurocentre Magendie, U1215, F-3300 Bordeaux, France

[2] MS Center Amsterdam, Anatomy and Neurosciences, Amsterdam Neuroscience, Amsterdam UMC Location VUmc, Amsterdam, The Netherlands

[3] Department of Diagnostic Imaging and Nuclear Medicine, Kyoto University Graduate School of Medicine, Kyoto, Japan

[4] Univ. Bordeaux, CNRS, UMR-5293, Groupe d'Imagerie Neurofonctionnelle, F-33000 Bordeaux, France

[5] CHU de Bordeaux, Unité neurovasculaire, F-33000 Bordeaux, France

[6] CHU de Bordeaux, Neuroimagerie diagnostique et thérapeutique, F-33000 Bordeaux, France

[7] Brain Connectivity and Behaviour Laboratory, Paris, France

Corresponding to:

- Thomas Tourdias, University of Bordeaux and Bordeaux University Hospital
- Email: thomas.tourdias@chu-bordeaux.fr
- Phone: +33(0)5 56 79 56 04

Abstract

Ischemic strokes disrupt brain networks, leading to remote effects in key regions like the thalamus, a critical hub for brain functions. However, non-invasive methods to quantify these remote consequences still need to be explored. This study aimed to demonstrate that MRI-derived R2* changes can capture iron accumulation linked with inflammation secondary to stroke-induced disconnection.

In order to link remote R2* changes to stroke-induced disconnection, we first conducted a secondary analysis of 156 prospectively included stroke patients who underwent MRI at baseline and 1-year follow-up. We mapped fibers disconnected by baseline infarcts to compare the R2* changes over 1 year according to the disconnectivity status in specific thalamic nuclei groups. We also identified the predictors of elevated R2* at 1 year in a multivariate context through linear regressions. In parallel, to understand the biological underpinning of the remote R2* changes, we set up a translational mouse model through photothrombotic induction of focal cortical infarcts or sham procedures in 110 C57BL/6J mice. We explored the mice through combinations of *in vivo* MRI at 72h, 2-, 4-, and 8-weeks, histology, qPCR for gene expression, mass spectrometry for iron concentration quantification, and additional *ex vivo* high-resolution diffusion tensor imaging.

In stroke patients, we found a significant increase of R2* within severely disconnected medial and lateral thalamic nuclei groups from baseline to 1 year. At the same time, no change occurred if these structures were not disconnected. We also showed that the disconnectivity status at baseline was a significant predictor of R2* at follow-up, independently from confounders, establishing a direct and independent relationship between baseline disconnection and the subsequent R2* increase within the associated locations. In mice, we recapitulated the patients' conditions by observing increased R2* in the stroke groups, specifically within the disconnected thalamic nuclei. Such remote and focal R2* changes peaked at 2 weeks, preceding and correlating with longer-term atrophy at 8 weeks. We established that the remote R2* increase was spatially and temporally correlated with a significant increase of chemically determined iron load bound to ferritin within activated microglial cells.

This study provides critical evidence that R2* is a sensitive marker of inflammation secondary to network disconnection, potentially informing future neuroprotective strategies targeting remote brain regions after stroke.

Introduction

Ischemic stroke is a major cause of severe long-term disability worldwide.[1] While revascularization strategies have led to significant improvements in outcomes,[2] more than one-third of stroke patients who achieve successful recanalization continue to experience persistent difficulties in daily activities and societal roles, despite achieving seemingly excellent functional outcomes (modified Rankin scale 0-1),[3] even among young adult stroke survivors.[4] These ongoing challenges are increasingly attributed to post-stroke cognitive and emotional impairments, which affect more than half of stroke survivors.[5,6] Such impairments in high-order functions may be linked to disrupted interactions between brain regions potentially due to the disconnection of central hubs.[7]

Some critical brain hubs, such as the thalamus or the substantia nigra, are essential to cognitive processes.[8-10] Although not directly affected by the most frequent middle cerebral artery infarcts as they lie outside this vascular territory, the thalamus and the substantia nigra are highly susceptible to disruption in the extensive thalamo-cortical projections[11] or nigro-striatal pathway.[12] This susceptibility means that damage caused by focal infarcts can lead to downstream effects in these hubs, impacting overall recovery. In consequence, alterations in regions remote from the initial infarct may display signs of injury influencing post-stroke outcomes, and present opportunities for neuroprotective interventions.[13] Quantifying these distant effects *in vivo* becomes critical for comprehensively understanding ischemic consequences and identifying potential biomarkers for future therapeutic trials.

Previously, we[14,15] and others[16] have reported secondary increase in R2* values detected by MRI, a quantitative metric sensitive to iron accumulation,[17] in brain areas remote from the initial infarct. While the anatomical stroke location and remote R2* increase suggest disconnection phenomena,[14,15] direct evidence linking remote R2* changes to network disconnection is still lacking. Moreover, the biological underpinning of these remote R2* changes after stroke remains poorly understood. The susceptibility effect of iron from hemoglobin and its degradation products following bleeding is the most important contributor to R2* changes in the brain.[18] Still, R2* might also be sensitive enough to capture high iron content within activated microglial cells in chronic inflammation as shown on MRI-to-pathological correlations from a subset of multiple sclerosis lesions[19] or in neurodegenerative conditions such as amyotrophic lateral sclerosis,[20] or progressive multifocal encephalopathy.[21]

Therefore, we hypothesize that similar histopathological changes might underlie *in vivo* observations in stroke patients, reflecting the consequences of network disconnection.

The aim of this study is to demonstrate that remote R2* changes following ischemic stroke reflect an increased iron content associated with inflammation secondary to stroke-inducted disconnection. To address this, we employed a combined approach involving a secondary analysis of clinical data and a translational mouse model.

Materials and methods

Clinical data analyses

Study population

In order to link remote R2* changes to stroke-induced disconnection, we performed a secondary analysis from a prospective study approved by the institutional ethics committee, with written informed consent from all participants, whose data have already been reported for other analyses (details in supplemental).

The study was conducted in a single center (Bordeaux, France) between June 2012 and February 2015 and enrolled participants according to the following criteria:

Primary inclusion criteria: *(i)* patients older than 18 years old; *(ii)* with a suspected clinical diagnosis of minor to severe supratentorial cerebral infarct [National Institutes of Health Stroke Scale (NIHSS) between 1 and 25]; and *(iii)* confirmed on diffusion-weighted imaging (DWI) at 24–72 h.

Exclusion criteria: *(i)* history of symptomatic cerebral infarct with functional deficit (pre-stroke modified Rankin Scale score $\geq$1; *(ii)* infratentorial infarct; (*iii)* history of severe cognitive impairment (dementia) or DSMIV axis 1 psychiatric disorders (except major depression); *(iv)* coma; *(v)* pregnant or breastfeeding females; and *(vi)* contraindications to MRI.

Participants underwent 3.0-T MRI scans (Discovery MR 750w; GE Healthcare) at 24-72 hours (baseline) and at 1 year (follow-up) using a consistent protocol including DWI, 3D-T1, and 2D-T2* multi-echo fast gradient echo sequences (details of parameters in supplemental).

We extracted a group of participants from this population without direct thalamic lesion (no thalamic infarct, no thalamic microbleed or hemorrhage) to explore the consequences of thalamic disconnection. We also extracted a group without direct substantia nigra lesion to examine the consequences of disconnection of this other major hub as supplementary analyses (Flowchart in **Supplementary Fig. 1**).

Image analyses

Baseline infarcts were delineated on DWI and coregistered to MNI-152 space. We generated disconnection probability maps using BCBtoolkit[22] which identified likely disconnected tracts

by comparing the infarcted regions against tractograms from 163 healthy subjects scanned at 7T, as reported before.[23] Disconnection maps were thresholded at 0.5, as a standard cut-off,[22] to include only fibers disconnected in more than half of the healthy subjects used to build the priors.

To assess thalamic disconnection, we overlaid such disconnection maps onto the main groups of thalamic nuclei (lateral, medial, and posterior) from an MNI-152 atlas[24] and classified patients as having "not disconnected," "mildly disconnected," or "severely disconnected" thalamic groups based on the amount of voxel overlap (details in Supplemental and **Supplementary Fig. 2 and 3**). We also explored the disconnection of substantia nigra similarly for supplementary analyses.

Then, R2* maps were generated from the voxel-by-voxel mono-exponential fitting of multi-echo T2* images and coregistered to MNI-152 space. We quantified the asymmetry index (AI) of R2* using the non-infarct side as an intrinsic control, as shown below.

$$AI = \frac{\mathrm{R2^*infarct\ side} - \mathrm{R2^*contralateral\ side}}{\mathrm{R2^*}infarct\ side + R2^*contralateral\ side} X\ 100$$

We reported the 95th percentile (AI_{95}), a metric reflecting the highest R2* values that has already been used before,[14,15] and that we compared within each thalamic nuclei group (and substantia nigra) according to their disconnectivity status.

Animal experiments

Animal model

In order to understand the biological substrate of the remote R2* changes, we set up a translational mouse model to recapitulate the observations from the patients.

We used a total of 110 C57BL/6J mice (8 weeks old, 20-25g) from Charles River Laboratories. Experiments were approved by the ethical committee (#28703, #30065 and#13152) and conducted in accordance with the European Directive (2010/63/EU).

We induced a right fronto-parietal cortical infarct sparing the thalamus *via* a photothrombotic ischemia.[25] We applied a cold light to the surface of the skull, 5 minutes after intraperitoneal injection of a Rose Bengal photosensitive dye (Aldrich Chemical Company, Milwaukee, USA) administered intraperitoneally at a dose of 10 µL/g body weight with a concentration of

5 mg/mL (details in supplemental). Sham-operated mice underwent the same surgical procedure and received the injection of Rose Bengal but without light exposure.

Stroke was confirmed by MRI at 72h. Then, analyses were targeted at 2-, 4-, and 8-weeks post-infarct among three groups (**Supplementary Fig. 4**):

- **Group 1**: Mice underwent sequential *in vivo* MRI before being sacrificed at 2-, 4-, and 8-weeks, followed by paraformaldehyde fixation for histological analyses.
- **Group 2**: Mice were sacrificed at 2-, 4-, and 8-weeks with fresh brain extraction for qPCR and mass spectrometry. All mice in this group also underwent *in vivo* MRI at a single time point before sacrifice, and these additional MRI data were pooled with those from Group 1.
- **Group 3**: Mice were examined with *ex vivo* high-resolution diffusion tensor MRI.

In vivo MRI acquisitions and analyses

Mice (n=69 from group 1 and group 2) underwent *in vivo* MRI on a 7T Bruker Biospec system at 72h, 2-, 4-, and 8-weeks, including DWI, 3D-TrueFISP, and 3D-multi echo T2* sequences (parameters in supplemental). Infarcts were outlined on DWI at 72h using 3D-Slicer. As in patients, R2* maps were generated and coregistered to a detailed mouse thalamic atlas[26] to quantify AI_{95} in specific nuclei and automatically extract their volumes (details in supplemental).

Biological analyses

Group 1 of mice (n=27) was sacrificed post-MRI for histological analyses. We stained for microglial cells (Iba1), astrocytes (GFAP), neurons (NeuN), and ferritin light chain. Immunoreactivity was quantified from images collected on a NanoZoomer microscope (40x objective) that captured full brain images through mosaic for direct comparison with MRI. Confocal microscopy (Leica DMI 6000) was also used to assess ferritin colocalization. Details of the procedures are in the supplemental.

Group 2 of mice (n=42) was sacrificed post-MRI for fresh brain extraction, followed by laser-micro-dissection of the thalamus. Briefly, brains were cut using 50 µm thick coronal sections on a freezing microtome (CM3050 S Leica) at -22 °C to prevent RNA degradation. Frozen sections were fixed in a series of precooled ethanol baths and stained with cresyl violet. Subsequently, sections were dehydrated, and a laser capture microdissection was performed

using a P.A.L.M MicroBeam microdissection system at 5x magnification. The whole thalamus was captured to maximize the amount of material and because the isolation of specific nuclei was challenging to conduct in such conditions. The material was split into separate adhesive caps to quantify gene expression and iron concentration in the same animal.

For gene expression, RNA was processed and analyzed according to an adaptation of published methods[27] (details in supplemental) to quantify RNA expression of the complement receptor 3 subunits (CD11b and CD18) that are only expressed by microglia cells,[28] but also heat shock proteins (HsP1) that are typically upregulated in response to oxidative stress,[29] and ferritin that is the main iron storage protein (Ftl1).[30]

For chemically determining iron concentration, we used inductively coupled mass spectrometry as a gold standard method that measures the total iron content regardless of its specific chemical form or the protein to which it is bound. We expressed the results in µg of iron per gram of dried brain tissue (details in supplemental).

Ex vivo MRI acquisitions and analyses

Group 3 of mice (n=41) underwent *ex vivo* long-scan acquisition (9 hours) on the 7T Bruker for high-resolution diffusion tensor imaging (parameters in supplemental). It included n=20 healthy mice and n=21 stroke mice explored at 2-, 4-, and 8-weeks post-stroke. We computed n=20 whole brain tractograms from the healthy mice which we filtered to extract the streamlines connecting the infarct region to the specific thalamic nuclei in the right hemisphere. After concatenating the 20 thalamo-cortical tracts, we obtained a right thalamo-cortical template which was mirrored across the interhemispheric plane to get a bilateral version. Then, in the n=21 stroke mice, we could measure fractional anisotropy changes along different positions of this template, ipsi- and contralateral to the infarct, at 2-, 4-, and 8-weeks post-stroke. More details are in the supplemental.

Statistical analyses

In patients, AI_{95} was compared between baseline and 1 year in each group of thalamic nuclei based on their disconnection status (not present, mild, severe) using the Wilcoxon signed-rank test. We also conducted voxel-based comparisons using the Brunner-Munzel test followed by false discovery rate correction. The association between AI_{95} at 1 year and disconnection was also assessed using a linear multivariate model adjusted for age, gender, baseline AI_{95}, and infarct volume as potential confounders.

In animals, AI_{95} within specific thalamic nuclei was first compared over time and between groups (stroke *vs*. sham) using 2-way ANOVA followed by post-hoc Tukey tests with p-values adjustment for multiple comparisons. AI_{95} within specific thalamic nuclei and their volumes were also correlated using Spearman's test. Histological quantifications were compared between stroke and sham groups using repeated Wilcoxon tests and Holm-Šídák correction for multiple comparisons. Fractional anisotropy was compared according to the position along the thalamocortical template and over time using 2-way ANOVA.

Analyses were conducted with GraphPad-Prsim (version 10.2.3) and R (version 4.0.5).

Results

Remote R2* increase and disconnection in patients

A total of 156 stroke participants (**Supplementary Fig. 1**) have been prospectively explored at baseline and after 1 year and included in the thalamus analysis (**Table 1**). We mapped each participant's white matter tracts disconnected by the infarct to assess whether disconnections involved specific thalamic nuclei groups. The anterior thalamic group was too small to run such analysis properly, and we focused on the lateral, medial, and posterior thalamic nuclei groups. Similarly, we also analyzed the disconnection status of the substantia nigra (**Supplementary Fig. 1** and **Supplementary Table 1**). Altogether, we could classify the thalamic nuclei and substantia nigra as "not disconnected", "mildly disconnected", or "severely disconnected" (**Supplementary Table 2**) to uniquely test the direct association between such disconnection status and remote R2* changes over 1 year.

Table 1: baseline characteristics of the participants included in the thalamus analysis

Variables	Participants included in the thalamus analysis (n=156)
Demographics	
Age (y)*	65 (56, 77)
Sex	
M	108 (69)
F	48 (31)
Hypertension	101 (65)
Diabetes mellitus	26 (17)
Active smoking	72 (46)
Body mass index (Kg/m^2)*	26.9 (24.1, 29.4)
Baseline visit	
NIHSS score*	3.0 (2.0, 6.0)
Time from onset to baseline MRI (h)*	46 (33, 59)
Recanalization procedure (thrombolysis and/or thrombectomy)	71 (46)
Infarct volume (mL)*	10 (2, 29)
Follow-up visit	
Time from onset to follow-up (y)*	1.0 (0.98, 1.01)

NIHSS score*	1.0 (0.0, 2.0)
Modified Rankin scale (mRS)*	1.0 (0.0, 2.0)

Except where indicated, data are numbers of patients with percentages in parentheses. * Data are median, with IQRs in parentheses.

Participants with severely disconnected lateral and medial thalamus showed significant AI_{95} increases from baseline to 1 year (median, -0.88 [IQR, -5.02-4.33] vs. 7.21 [IQR, 1.30-13.8]; p<0.001 and median, -1.19 [IQR, -3.96-2.00] vs. 4.57 [IQR, -1.35-8.29]; p<0.001 for lateral and medial groups respectively) while, importantly, no significant AI_{95} changes were observed if these structures were not or mildly disconnected (**Fig. 1A**). The voxel-based analysis confirmed that clusters of AI_{95} increases from baseline to 1 year were only found in the groups of severely disconnected lateral and medial thalamus (**Fig. 1B**). Similar AI_{95} increases were observed in participants with severely disconnected substantia nigra but not otherwise (**Supplementary Fig. 5**). We found no significant AI_{95} variation according to the disconnection status within the posterior thalamus, but nevertheless, the voxel-based analysis revealed clusters of voxels with significantly higher values in sub-regions of the posterior thalamus only in severely disconnected participants (**Fig. 1B**).

The qualitative review revealed that focal areas of high R2* could also be identified by simple visual inspection on follow-up MRI, but only for participants with severely disconnected thalamic groups (**Fig. 1C**).

To ensure that the disconnection status was truly a predictor of R2* at 1 year independently from confounders such as baseline AI_{95} or stroke volume, we also ran multivariate linear regression analyses. It showed that disconnection severity was a significant and independent predictor of AI_{95} at 1 year for the lateral (p=0.002) and medial thalamus (p<0.001; **Table 2**), and substantia nigra (p=0.004; **Supplementary Table 3**).

Overall, these results established a direct and independent relationship between baseline disconnection and subsequent R2* increases, specifically in the disconnected structures.

Table 2: Multivariable linear regression models for prediction of AI_{95} at 1 year in each group of thalamic nuclei.

Variable	B value (95%CI)	*P* Value
Disconnection of LATERAL group of thalamic nuclei		
Age (+1 y)	-0.04 (-0.09, 0.01)	0.10
Sex (F)	-0.48 (-1.9, 0.96)	0.50

AI_{95} at baseline (+ 1)	**0.28 (0.16, 0.40)**	**<0.001*** **
Infarct volume (+ 1 mL)	0.01 (-0.01, 0.02)	0.30
Disconnection		
Mildly disconnected	-0.62 (-2.4, 1.2)	0.50
Severely disconnected	**2.9 (1.1, 4.7)**	**0.002****
Disconnection of MEDIAL group of thalamic nuclei		
Age (+1 y)	**-0.07 (-0.13, -0.01)**	**0.013***
Sex (F)	-1.0 (-2.6, 0.57)	0.20
AI_{95} at baseline (+ 1)	**0.36 (0.24, 0.48)**	**<0.001*** **
Infarct volume (+ 1 mL)	**0.05 (0.04, 0.07)**	**<0.001*** **
Disconnection		
Mildly disconnected	0.87 (-3.1, 1.3)	0.40
Severely disconnected	**5.2 (2.9, 7.5)**	**<0.001*** **
Disconnection of POSTERIOR group of thalamic nuclei		
Age (+1 y)	0.01 (-0.04, 0.06)	0.60
Sex (F)	-1.3 (-2.7, 0.16)	0.081
AI_{95} at baseline (+ 1)	**0.14 (0.01, 0.27)**	**0.038***
Infarct volume (+ 1 mL)	**0.03 (0.01, 0.04)**	**0.001****
Disconnection		
Mildly disconnected	0.07 (-1.8, 1.9)	0.90
Severely disconnected	0.88 (-1.0, 2.8)	0.40

Dynamic of remote R2* increase in the animal model

As pathological tissues are not collected in stroke patients, we set up a mouse model recapitulating the human observations, which we could use to assess the biological underpinning. The adapted photothrombosis model produced reproducible lesions with restricted diffusion in the sensorimotor cortex (**Supplementary Fig. 6**), leading to high T2 signal at 72 hours, followed by progressive cortical atrophy, resembling typical human cortical stroke (**Fig. 2A**). Infarcts always spared the thalamus. There were no lesions in sham-operated mice.

Visual inspection consistently revealed focal thalamic R2* increases at 2- and 4-week post-stroke, with subtler changes at 8-weeks (**Fig. 2B**). Co-registration with a thalamic atlas (26) localized R2* increases specifically within the ventral posterolateral (VPL) and ventral posteromedial (VPM) nuclei (**Fig. 3A**). Quantification of AI_{95} within these nuclei showed a

significant increase in stroke mice compared to sham (group effect, p=0.019 and 0.009 in VPL and VPM, respectively), with distinct temporal dynamics (group x time interactions p<0.05) peaking at 2 and 4 weeks for the stroke mice (**Fig. 3B**). Additionally, we measured significant ipsilateral volume loss in VPL and VPM in stroke mice compared to sham (group effect, p=0.008 and 0.04 in VPL and VPM respectively), worsening progressively in stroke but not in sham mice (group x time interactions p<0.05) and becoming prominent at 8-week follow-up (**Fig. 3C**). As an additional control, we also identified three distant thalamic nuclei (AND, IDN, LH) with volumes close to those of VPL and VPM but distinct thalamo-cortical projections, and found no significant AI_{95} or volume changes over time in these nuclei in stroke mice compared to sham.

The mice followed longitudinally with repeated MRIs until 8 weeks provided the unique opportunity to directly correlate R2* and volume changes over time within the same animals. Such analysis revealed that the R2* increases in VPL and VPM at 2 weeks (the peak of the time-course curve) were significantly correlated with subsequent atrophy measured at 8 weeks (**Fig. 3D**; r, -0.72; [95%CI, -0.89, -0.33]; p=0.0024).

Overall, these results revealed that remote and focal R2* increase can be modeled through experimental cortical stroke in mice, resembling closely the human pattern, and they showed that R2* increase preceded and predicted longer term atrophy.

Biological substrate of remote R2* increase

We ran histology and molecular biology to elucidate the modifications associated with the remote R2* increase. Histological analyses at 2-, 4-, and 8-weeks post-stroke, conducted immediately after MRI scans, showed glial cell activation in regions delineating precisely VPL and VPM in close correspondence with the observed R2* increases in MRI (**Fig. 4A**). We also found astrocytic reactivity with increased GFAP staining at all time points, alongside the microglial activation evidenced by larger cell bodies and thicker processes that translated into significant Iba1 staining increases (**Fig. 4B and 5A**). Notably, the mRNA expression level of the microglia-specific receptor of the complement (CD11b and CD18 sub-units), which is a marker of microglial activation, peaked at 2- and 4-weeks, which also came with a significant mRNA increase of heat shock protein-1 at 2 weeks (**Fig. 5B**). Neuronal count decreased progressively until marked reduction, aligning with MRI-measured atrophy at 8 weeks (**Fig. 5A**).

The specific quantification of iron via mass spectrometry in laser microdissected thalamus tissue ipsilateral to stroke showed significantly increased total iron load at 2 and 4 weeks that didn't reach significance at 8 weeks (**Fig. 5C**). The mRNA expression of ferritin, the primary iron storage protein, was significantly increased at these time points (**Fig. 5C**), with confocal microscopy showing ferritin localization within the activated microglial cells (**Fig. 4B**).

In total, these results established that the remote R2* measured *in vivo* was spatially and temporally correlated with higher iron load mainly bound to ferritin within pro-inflammatory microgial cells.

Remote R2*increase and disconnection in mice

We collected high-resolution diffusion MRI to ensure that the remote VPL and VPM modifications described above during the follow-up were directly related to thalamo-cortical projection disruption. In healthy mice, we extracted a white matter pathway connecting the cortical stroke site to ipsilateral VPL and VPM within the thalamus, indicating a direct connection between these regions. This tract passed below the lateral ventricle, crossed the distal part of the corpus callosum, ran between the caudate and putamen before reaching specifically the VPL and VPM thalamic nuclei (**Fig. 6A**) corresponding well with specific dye injection within VPL and VPM from the Allen Brain Atlas (**Supplementary Fig. 7**).

We used this pathway as a template to quantify microstructural changes in stroke mice. On the contralateral side (left), fractional anisotropy varied significantly according to the position along the tract (position effect, $p<0.0001$) in line with the anatomical characteristics of this bundle, but showed no time-dependent changes following stroke. On the stroke side, we found significant time-dependent variations ($p=0.003$) that differed according to the position within the tract (time x position interaction, $p<0.001$). Notably, at the higher anisotropy position close to the tract midpoint, fractional anisotropy decreased significantly from 2 to 4 weeks which was followed by partial recovery at 8 weeks, though not reaching 2-week levels (**Fig. 6B**).

These results confirmed that the R2* changes within VPL and VPM were related specifically to stroke-induced disconnection as the microstructure of the direct connecting pathway was significantly altered.

Discussion

Brain functions emerge from dynamic interactions between areas connected by white matter tracts.[7] Ischemic strokes disrupt these connections, leading to remote effects that are challenging to quantify *in vivo*. In this translational study, we demonstrate that remote R2* increases occur specifically in disconnected structures, such as thalamic nuclei or substantia nigra. We also showed that these R2* increases reflect iron-rich microglial activation, which precedes and predicts secondary atrophy. This suggests that iron imaging can provide a comprehensive view of remote stroke consequences and potentially inform future neuroprotective strategies.

Remote changes in regions distant from focal cortical strokes, particularly in the thalamus or the substantia nigra, have been reported for many years through a variety of imaging approaches[31-34] with R2* having the potential to capture the long-term modifications.[14,15] Traditionally attributed to anterograde or retrograde degeneration based on anatomical presumptions, these changes have lacked direct evidence linking them to fiber disconnection. By mapping focal infarct lesions onto high-resolution connectomes,[22,23] we could quantitatively measure R2* changes for the first time in specific hub regions that have been disconnected or not according to the initial infarct location. This demonstrated that the delayed R2* reaches significant increase only following substantial disconnection. The posterior thalamus behaved differently from the lateral and medial group or the substantia nigra which will require further explorations. One potential explanation could be that the type of secondary degeneration depends on the amount of afferent versus efferent pathways. Interestingly, the pulvinar shows mainly dense efferent projections (output) to cortical regions while the medial and lateral thalamic nuclei groups, as well as the substantia nigra, have a more balanced afferent (input) and efferent (output) connectivity pattern[8,12] that could produce more extensive degeneration.

Additionally, using diffusion MRI in mice, we reconstructed a thalamo-cortical pathway between experimentally induced cortical infarcts and altered thalamic nuclei, directly demonstrating microstructural alterations within bundles connecting affected nuclei. The reduction in fractional anisotropy at 4 weeks aligns with axonal fragmentation, as seen in spinal cord degeneration[35] while subsequent glial proliferation and cellular debris may contribute to the partial recovery of fractional anisotropy observed at 8 weeks.[36]

The translational approach in mice further evidenced that R2* captures inflammatory responses in disconnected regions. Histological analyses[37] and *in vivo* PET imaging studies with tracers for the peripheral benzodiazepine receptors[38] have shown that microglial activation is a key feature of secondary injuries. We confirmed strong microglial activation markers in the disconnected VPL and VPM nuclei, which correlated tightly with increased R2* on MRI, in both spatial and temporal dimensions. Mass spectrometry data indicated that elevated R2* values reflect increased total iron content, likely bound to upregulated ferritin within activated microglial cells. This finding aligns with paramagnetic effects seen in amyotrophic lateral sclerosis[20] and progressive multifocal leukoencephalopathy,[21] where iron-rich microglial cells have been implicated in specimen analyses. Our observation is also reminiscent of a particular histological subtype of multiple sclerosis lesions called the "chronic active lesions" that are characterized by a demyelinating core surrounded by a dense rim of activated microglial cells.[39] Interestingly, the so called "paramagnetic rim lesion, PRL" on susceptibility sequences emerged as an appealing *in vivo* MRI marker for these chronic active lesions[40] with the source of the signal of the rim being molecular iron sequestered intracellularly and bound to ferritin within pro-inflammatory macrophages and microglia.[19] Here, we extend the role of R2* as a marker of neuroinflammation in secondary degeneration post-stroke. Imaging allowed us to trace the inflammatory response over time non-invasively showing, in mice, a delayed onset, peaking between 2-4 weeks and declining at 8 weeks, consistent with more complex PET-based or invasive histological analyses in other models.[41,42] Importantly, R2* was sensitive enough to capture subtle inter-individual differences despite the standardized induction of the model, and served as an earlier biomarker than atrophy, representing the late and irreversible stage of neurodegeneration. The correlation between R2* and subsequent atrophy implies a potential causal relationship between activated microglia and neurodegeneration, potentially involving oxidative stress mechanisms, supported by the upregulation of heat shock proteins. This is further corroborated by the recent identification of a neurodegenerative subtype of microglia ($CD11c^{+}$) in the disconnected thalamus.[43] Our findings in stroke patients closely parallel those in the mouse model, indicating that R2* iron imaging could serve as a valuable biomarker to quantify and monitor remote stroke consequences, preceding neuronal loss as measured from flumazenil PET[34] or atrophy.[44]

In spite of these promising results, our study was limited by the absence of behavioral data, which made it underpowered to demonstrate behavioral correlates to remote changes.

However, previous works have linked delayed injury to cognitive and emotional deficits.[14,45] In patients, we relied on indirect disconnectome methods rather than direct diffusion tensor imaging, which may have limited our ability to perfectly assess individual disconnection. However, such indirect disconnectivity method has been extensively validated.[22,23,46] In animals, we haven't identified iron directly in histological sections through Perls Prussian blue staining, but we used the gold standard mass spectrometry in microdissected tissue that is the only able to provide true quantitative measurement. Finally, the metabolic pathways of iron sequestration haven't been explored and whether iron accumulation is causally involved in the associated neurodegeneration, for instance through ferroptosis,[47] is an ongoing area of investigation which could be the focus of future research.

In conclusion, a remote increase in R2* in disconnected brain structures following stroke represents neuroinflammation that precedes neuronal loss. This imaging biomarker could be crucial for advancing neuroprotective trials aimed at preserving brain networks.[48]

Data availability

The tabulated data that support the findings of this study are available from the corresponding author, upon reasonable request from a qualified investigator.

Acknowledgements

We thank the contribution of the AEM2 Platform (Martine Ropert-Bouchet, University of Rennes 1 / Biochemistry Laboratory, University Rennes Hospital) for mass spectrometry and the contribution of the PUMA platform (Thierry Lesté-Lasserre and Marlène Maître, Neurocentre Magendie, INSERM U1215) for laser microdissection and quantitative PCR. The MRI acquisitions were performed at the Institute of Bioimaging (UAR 3767), and the microscopy was done in the Bordeaux Imaging Center, a service unit of the CNRS-INSERM and Bordeaux University, both members of the national infrastructure France BioImaging supported by the French National Research Agency (ANR-10-INBS-04).

Funding

This work was supported by the University of Bordeaux's IdEx 'Investments for the Future' program RRI 'IMPACT', and the IHU 'Precision & Global Vascular Brain Health Institute – VBHI' funded by the France 2030 initiative (ANR-23-IAHU-0001). This work was also granted by the Thérèse and René Planiol foundation. In addition, TT received financial support from the French ministry of Health for the clinical trial CHEL-IC (clinical trial registration No. NCT05111821). M.T.d.S is supported by HORIZON- INFRA-2022 SERV (Grant No. 101147319) "EBRAINS 2.0: A Research Infrastructure to Advance Neuroscience and Brain Health", by the European Union's Horizon 2020 research and innovation programme under the European Research Council (ERC) Consolidator grant agreement No. 818521 (DISCONNECTOME).

Competing interests

The authors report no competing interests.

Figure captions

Figure 1: Relationship between disconnectivity and secondary R2* increase at 1-year follow-up in patients.

(A) shows the evolution of AI_{95} from baseline to 1 year, categorized by disconnectivity status for the lateral, medial, and posterior groups of thalamic nuclei. **(B)** presents the voxel-based comparisons with color-coded clusters that showed a significant increase from baseline to 1 year. **(C)** presents individual examples of severely disconnected cases, showing baseline diffusion images and corresponding R2* map at 1-year follow-up. White arrows point toward focal thalamic R2* increases on the stroke-affected side compared to the contralateral side, magnified below with a delineation of the thalamic groups where the highest asymmetry was measured. For reference, corresponding Morel atlas plates delineate the affected groups of thalamic nuclei. Of note, the focal R2* increase within the medial group (blue) is also associated with a visible increase in the small anterior group (purple).

Figure 2: Dynamic evolution of stroke and R2* in the mouse model.

(A) displays T2-weighted images and **(B)** R2* maps in a sham-operated and a stroke mouse followed longitudinally with repeated MRI at 72h, 2-, 4-, and 8-weeks. The focal infarct, indicated by the red asterisk, is clearly visible at 72 hours and evolves into focal atrophy with passive dilatation of the ipsilateral ventricle (**). R2* maps show higher values within iron-rich myelinated white matter tracts, such as the corpus callosum (white arrows) and internal capsules (white arrowheads). At 2 and 4 weeks, a focal area with R2* increase appears in the thalamus ipsilateral to the stroke and becomes subtler at the 8-week follow-up (red arrows).

Figure 3: Quantification of R2* and thalamic volumes over time in the mouse model

(A) provides an example of R2* map co-registration with the thalamic atlas (26). Two different z-positions are displayed from a stroke-induced mouse at 2 weeks. The stroke is marked with a red asterisk. Focal R2*increases are visually identified (red arrows, magnified in insets). Among all the thalamic nuclei (top row), we observed that the focal R2* increases were precisely located within VPL (green) and VPM (red) nuclei, which are the only two nuclei maintained in the bottom row.

(B) shows the time course of R2* quantification using AI_{95} and **(C)** presents the time course of VPL and VPM volumes for stroke (orange) and sham-operated (green) mice. In stroke mice, R2*peaks at 2 weeks, while volumes progressively decrease until 8 weeks. **(D)** shows a significant inverse correlation between R2* at 2 weeks within VPL and VPM and the volumes of these nuclei at 8-week follow-up. Error bars indicate mean ± SEM. *, $p \leq 0.05$; **, $p \leq 0.01$; and ***, $p \leq 0.001$ from Tukey post-hoc tests of stroke vs. sham with p values adjusted for multiple comparisons.

Figure 4: Histological-to-MRI comparison

(A) shows immunostaining of microglial cells (green) and neurons (red) with blue nuclear counterstain (DAPI) alongside the corresponding R2* map acquired prior to sacrifice. Enlarged views highlight microglial activation within the ventral posterolateral (VPL) and ventral posteromedial (VPM) thalamic nuclei (dotted lines), spatially correlated with the focal R2*increase. **(B)** displays higher magnification confocal images of microglial cells (red) and ferritin light chain (green), demonstrating ferritin localization within activated microglia, which exhibit enlarged cell bodies and thicker processes. The scale bar is 100 µm.

Figure 5: **Quantification of immunostaining, gene expression, and iron concentration**

(A) presents the semi-quantitative analysis of microglia (Iba1), astrocytes (GFAP), and neurons (NeuN) immunoreactivity over time, expressed as the percentage of area stained above an identical threshold on the stroke side compared to the contralateral side. **(B)** shows relative gene expression levels in stroke (orange) compared to sham (green). **(C)** displays iron-related markers with ferritin gene expression and iron concentration from mass spectrometry, both extracted from laser-capture microdissections of the thalamus where the high R2* spots (red arrow) have been observed. Error bars indicate mean ± SEM. *, $p \leq 0.05$; and **, $p \leq 0.01$ from Wilcoxon tests and Holm-Šídák correction for multiple comparisons.

Figure 6: Thalamo cortical fibers connecting stroke site to VPL and VPM from ex vivo diffusion MRI

(A) shows a 3D projection of MR tractography between the stroke site and VPL / VPM. Colors indicate tract directions: green for rostro-caudal, red for left-right, and blue for dorsal-ventral. The bottom panel shows segmentations of these thalamocortical tracts in 16 evenly distributed segments color-coded by position. **(B)** depicts fractional anisotropy quantification in stroke mice on the stroke (right) and contralateral side (left) at 2, 4 and 8 weeks, with quantification conducted within the 16 segments indicated on the abscissa and color-coded by position as in A.

References

1. Collaborators GBDS. Global, regional, and national burden of stroke and its risk factors, 1990-2019: a systematic analysis for the Global Burden of Disease Study 2019. Lancet Neurol. 2021;20(10):795-820.

2. Goyal M, Menon BK, van Zwam WH, et al. Endovascular thrombectomy after large-vessel ischaemic stroke: a meta-analysis of individual patient data from five randomised trials. Lancet. 2016;387(10029):1723-31.

3. Gadidi V, Katz-Leurer M, Carmeli E, Bornstein NM. Long-term outcome poststroke: predictors of activity limitation and participation restriction. Arch Phys Med Rehabil. 2011;92(11):1802-8.

4. Skajaa N, Adelborg K, Horvath-Puho E, et al. Labour market participation and retirement after stroke in Denmark: registry based cohort study. BMJ. 2023;380:e072308.

5. Kapoor A, Lanctot KL, Bayley M, et al. "Good Outcome" Isn't Good Enough: Cognitive Impairment, Depressive Symptoms, and Social Restrictions in Physically Recovered Stroke Patients. Stroke. 2017;48(6):1688-90.

6. Saar K, Tolvanen A, Poutiainen E, Aro T. Returning to Work after Stroke: Associations with Cognitive Performance, Motivation, Perceived Working Ability and Barriers. J Rehabil Med. 2023;55:jrm00365.

7. Thiebaut de Schotten M, Forkel SJ. The emergent properties of the connected brain. Science. 2022;378(6619):505-10.

8. Halassa M. The thalamus: Cambridge University press, 2023.

9. Saalmann YB, Kastner S. The cognitive thalamus. Front Syst Neurosci. 2015;9:39.

10. Gupta S, Khan J, Ghosh S. Molecular mechanism of cognitive impairment associated with Parkinson's disease: A stroke perspective. Life Sci. 2024;337:122358.

11. Behrens TE, Johansen-Berg H, Woolrich MW, et al. Non-invasive mapping of connections between human thalamus and cortex using diffusion imaging. Nat Neurosci. 2003;6(7):750-7.

12. Zhang Y, Larcher KM, Misic B, Dagher A. Anatomical and functional organization of the human substantia nigra and its connections. Elife. 2017;6.

13. Duering M, Schmidt R. Remote changes after ischaemic infarcts: a distant target for therapy? Brain. 2017;140(7):1818-20.

14. Kuchcinski G, Munsch F, Lopes R, et al. Thalamic alterations remote to infarct appear as focal iron accumulation and impact clinical outcome. Brain. 2017;140(7):1932-46.

15. Linck PA, Kuchcinski G, Munsch F, et al. Neurodegeneration of the Substantia Nigra after Ipsilateral Infarct: MRI R2* Mapping and Relationship to Clinical Outcome. Radiology. 2019;291(2):438-48.

16. van Etten ES, van der Grond J, Dumas EM, van den Bogaard SJ, van Buchem MA, Wermer MJ. MRI Susceptibility Changes Suggestive of Iron Deposition in the Thalamus after Ischemic Stroke. Cerebrovasc Dis. 2015;40(1-2):67-72.

17. Langkammer C, Krebs N, Goessler W, et al. Quantitative MR imaging of brain iron: a postmortem validation study. Radiology. 2010;257(2):455-62.

18. Jain A, Malhotra A, Payabvash S. Imaging of Spontaneous Intracerebral Hemorrhage. Neuroimaging Clin N Am. 2021;31(2):193-203.

19. Absinta M, Maric D, Gharagozloo M, et al. A lymphocyte-microglia-astrocyte axis in chronic active multiple sclerosis. Nature. 2021;597(7878):709-14.

20. Kwan JY, Jeong SY, Van Gelderen P, et al. Iron accumulation in deep cortical layers accounts for MRI signal abnormalities in ALS: correlating 7 tesla MRI and pathology. PLoS One. 2012;7(4):e35241.

21. Mahajan KR, Amin M, Poturalski M, et al. Juxtacortical susceptibility changes in progressive multifocal leukoencephalopathy at the gray-white matter junction correlates with iron-enriched macrophages. Mult Scler. 2021;27(14):2159-69.

22. Foulon C, Cerliani L, Kinkingnehun S, et al. Advanced lesion symptom mapping analyses and implementation as BCBtoolkit. Gigascience. 2018;7(3):1-17.

23. Thiebaut de Schotten M, Foulon C, Nachev P. Brain disconnections link structural connectivity with function and behaviour. Nat Commun. 2020;11(1):5094.

24. Saranathan M, Iglehart C, Monti M, Tourdias T, Rutt B. In vivo high-resolution structural MRI-based atlas of human thalamic nuclei. Sci Data. 2021;8(1):275.

25. Labat-gest V, Tomasi S. Photothrombotic ischemia: a minimally invasive and reproducible photochemical cortical lesion model for mouse stroke studies. J Vis Exp. 2013(76).

26. Hikishima K, Komaki Y, Seki F, Ohnishi Y, Okano HJ, Okano H. In vivo microscopic voxel-based morphometry with a brain template to characterize strain-specific structures in the mouse brain. Sci Rep. 2017;7(1):85.

27. Bustin SA, Benes V, Garson JA, et al. The MIQE guidelines: minimum information for publication of quantitative real-time PCR experiments. Clin Chem. 2009;55(4):611-22.

28. Aguzzi A, Barres BA, Bennett ML. Microglia: scapegoat, saboteur, or something else? Science. 2013;339(6116):156-61.

29. Yan LJ, Christians ES, Liu L, Xiao X, Sohal RS, Benjamin IJ. Mouse heat shock transcription factor 1 deficiency alters cardiac redox homeostasis and increases mitochondrial oxidative damage. EMBO J. 2002;21(19):5164-72.

30. Zecca L, Youdim MB, Riederer P, Connor JR, Crichton RR. Iron, brain ageing and neurodegenerative disorders. Nat Rev Neurosci. 2004;5(11):863-73.

31. Herve D, Molko N, Pappata S, et al. Longitudinal thalamic diffusion changes after middle cerebral artery infarcts. J Neurol Neurosurg Psychiatry. 2005;76(2):200-5.

32. Li C, Ling X, Liu S, et al. Early detection of secondary damage in ipsilateral thalamus after acute infarction at unilateral corona radiata by diffusion tensor imaging and magnetic resonance spectroscopy. BMC Neurol. 2011;11:49.

33. Winter B, Brunecker P, Fiebach JB, Jungehulsing GJ, Kronenberg G, Endres M. Striatal Infarction Elicits Secondary Extrafocal MRI Changes in Ipsilateral Substantia Nigra. PLoS One. 2015;10(9):e0136483.

34. Yamauchi H, Kagawa S, Kusano K, Ito M, Okuyama C. Neuronal Alterations in Secondary Thalamic Degeneration Due to Cerebral Infarction: A (11)C-Flumazenil Positron Emission Tomography Study. Stroke. 2022;53(10):3153-63.

35. Kerschensteiner M, Schwab ME, Lichtman JW, Misgeld T. In vivo imaging of axonal degeneration and regeneration in the injured spinal cord. Nat Med. 2005;11(5):572-7.

36. Beaulieu C, Does MD, Snyder RE, Allen PS. Changes in water diffusion due to Wallerian degeneration in peripheral nerve. Magn Reson Med. 1996;36(4):627-31.

37. Cao Z, Harvey SS, Bliss TM, Cheng MY, Steinberg GK. Inflammatory Responses in the Secondary Thalamic Injury After Cortical Ischemic Stroke. Front Neurol. 2020;11:236.

38. Gerhard A, Schwarz J, Myers R, Wise R, Banati RB. Evolution of microglial activation in patients after ischemic stroke: a [11C](R)-PK11195 PET study. Neuroimage. 2005;24(2):591-5.

39. Kuhlmann T, Ludwin S, Prat A, Antel J, Bruck W, Lassmann H. An updated histological classification system for multiple sclerosis lesions. Acta Neuropathol. 2017;133(1):13-24.

40. Absinta M, Sati P, Reich DS. Advanced MRI and staging of multiple sclerosis lesions. Nat Rev Neurol. 2016;12(6):358-68.

41. Anttila JE, Albert K, Wires ES, et al. Post-stroke Intranasal (+)-Naloxone Delivery Reduces Microglial Activation and Improves Behavioral Recovery from Ischemic Injury. eNeuro. 2018;5(2).

42. Arlicot N, Petit E, Katsifis A, et al. Detection and quantification of remote microglial activation in rodent models of focal ischaemia using the TSPO radioligand CLINDE. Eur J Nucl Med Mol Imaging. 2010;37(12):2371-80.

43. Cao Z, Harvey SS, Chiang T, et al. Unique Subtype of Microglia in Degenerative Thalamus After Cortical Stroke. Stroke. 2021;52(2):687-98.

44. Tamura A, Tahira Y, Nagashima H, et al. Thalamic atrophy following cerebral infarction in the territory of the middle cerebral artery. Stroke. 1991;22(5):615-8.

45. Fernandez-Andujar M, Doornink F, Dacosta-Aguayo R, et al. Remote thalamic microstructural abnormalities related to cognitive function in ischemic stroke patients. Neuropsychology. 2014;28(6):984-96.

46. Talozzi L, Forkel SJ, Pacella V, et al. Latent disconnectome prediction of long-term cognitive-behavioural symptoms in stroke. Brain. 2023.

47. Fuhrmann DC, Brune B. A graphical journey through iron metabolism, microRNAs, and hypoxia in ferroptosis. Redox Biol. 2022;54:102365.

48. Tennant KA, Taylor SL, White ER, Brown CE. Optogenetic rewiring of thalamocortical circuits to restore function in the stroke injured brain. Nat Commun. 2017;8:15879.

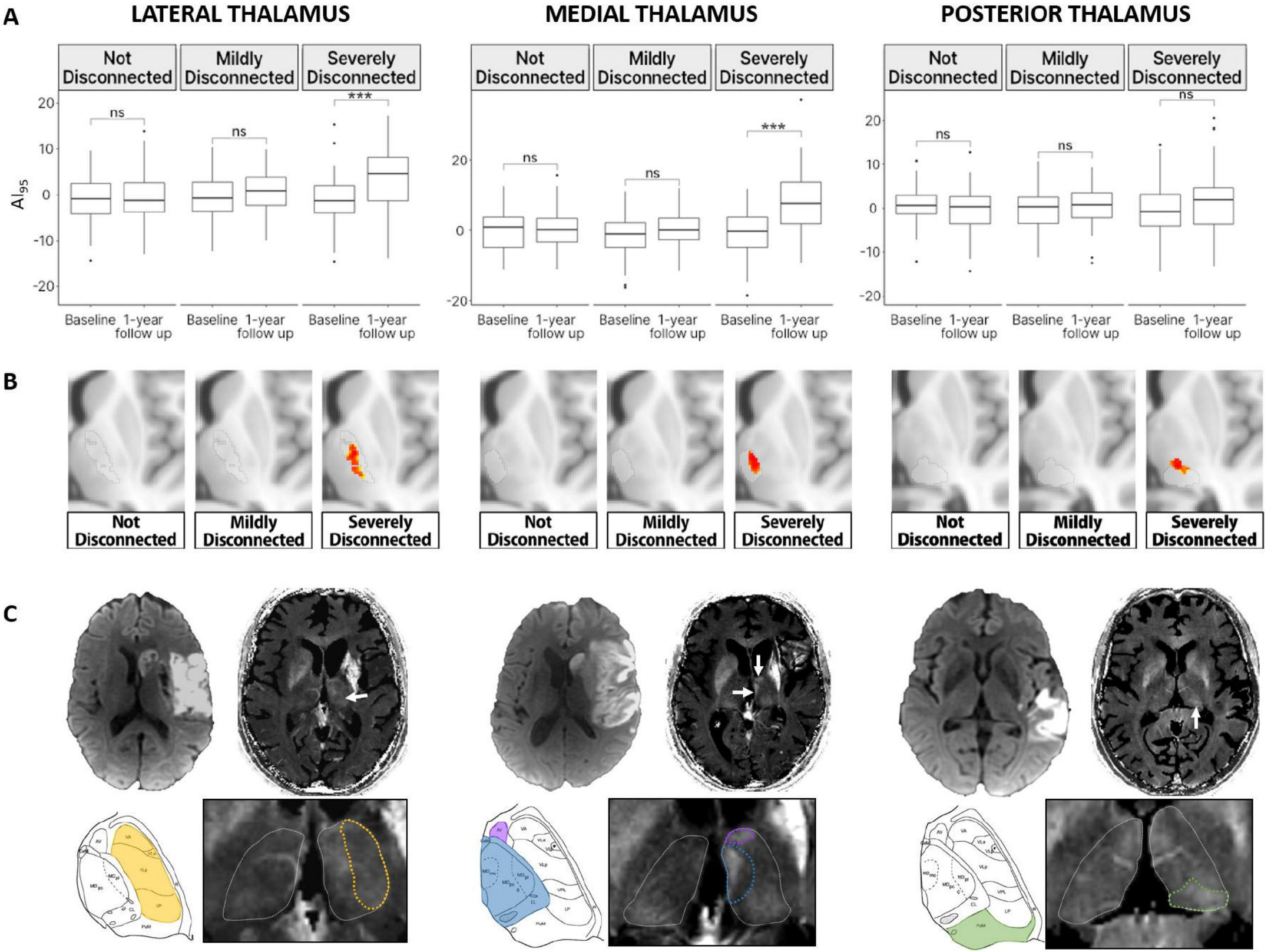
A
LATERAL THALAMUS
MEDIAL THALAMUS
POSTERIOR THALAMUS
Not Disconnected
Mildly Disconnected
Severely Disconnected
AI_{95}
ns
***
Baseline
1-year follow up
B
C

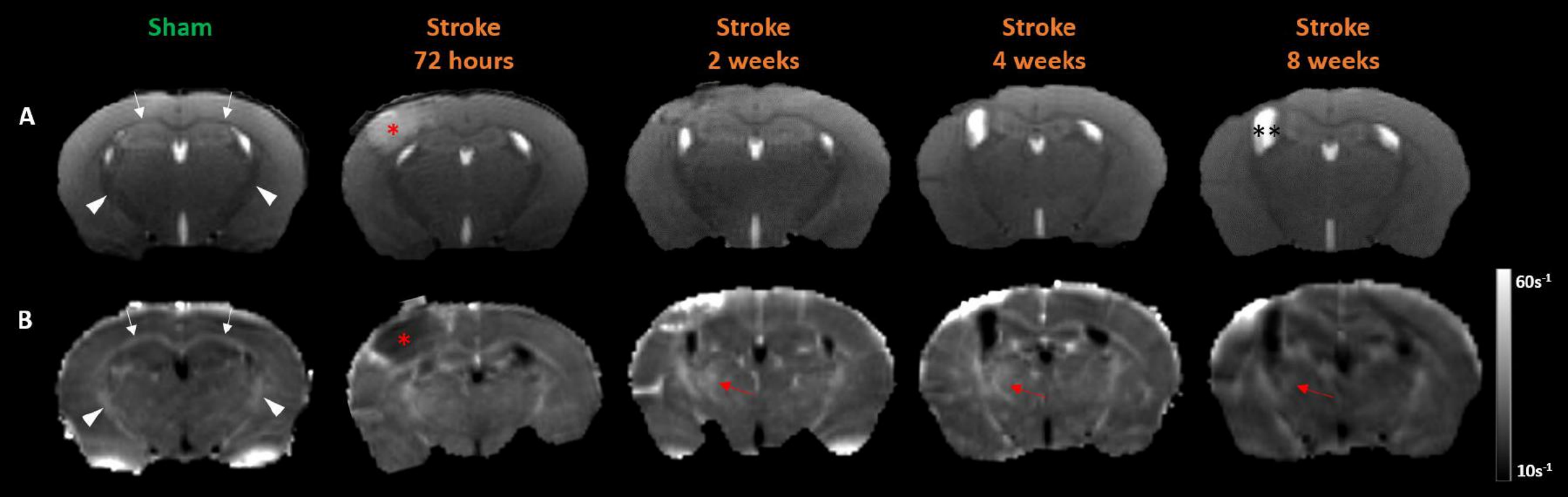
Sham
Stroke
72 hours
Stroke
2 weeks
Stroke
4 weeks
Stroke
8 weeks
A
B
60s-1
10s-1

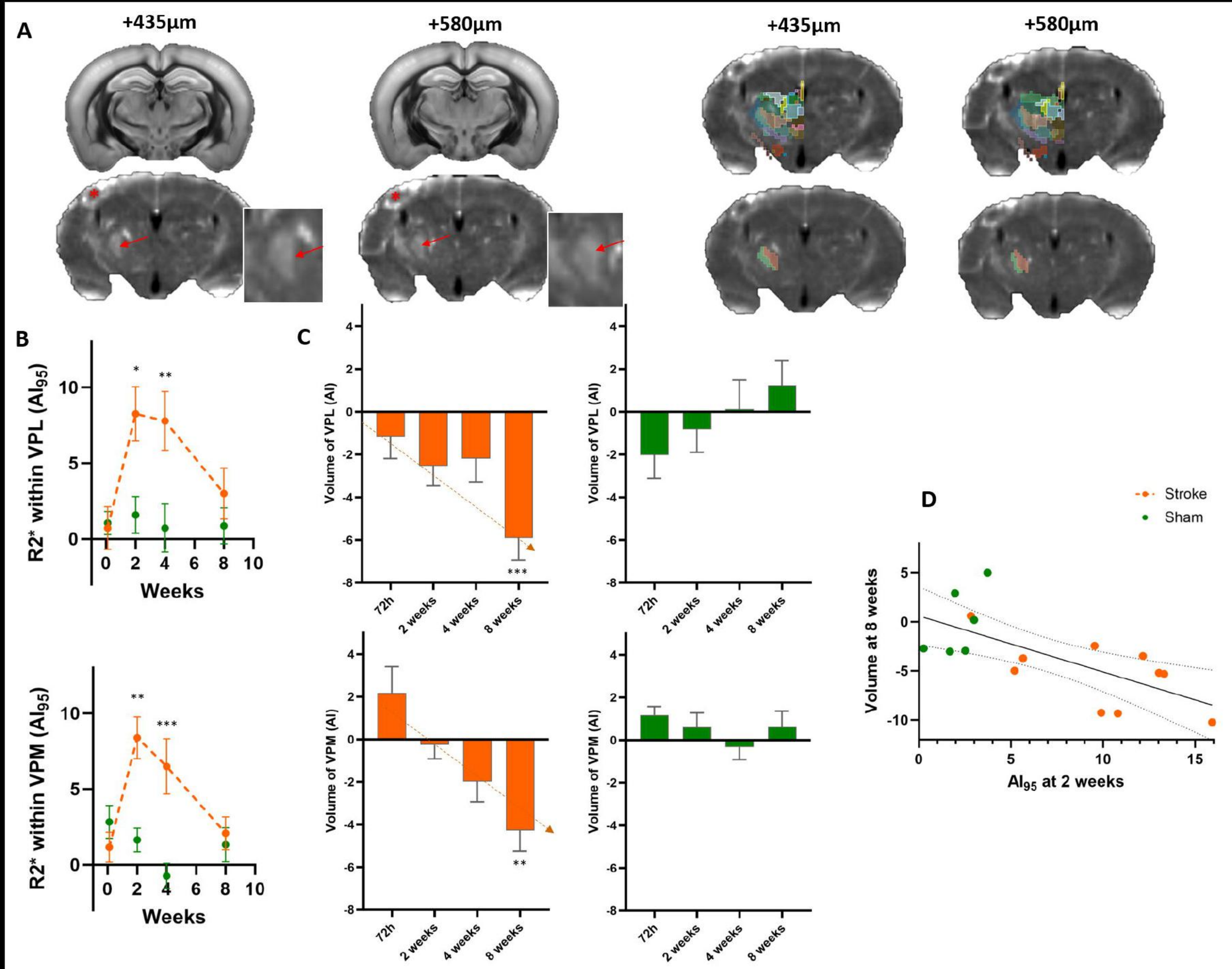
A
+435µm
+580µm
+435µm
+580µm
B
R2* within VPL (AI95)
Weeks
R2* within VPM (AI95)
Weeks
C
Volume of VPL (AI)
Volume of VPM (AI)
72h
2 weeks
4 weeks
8 weeks
D
Stroke
Sham
Volume at 8 weeks
AI95 at 2 weeks

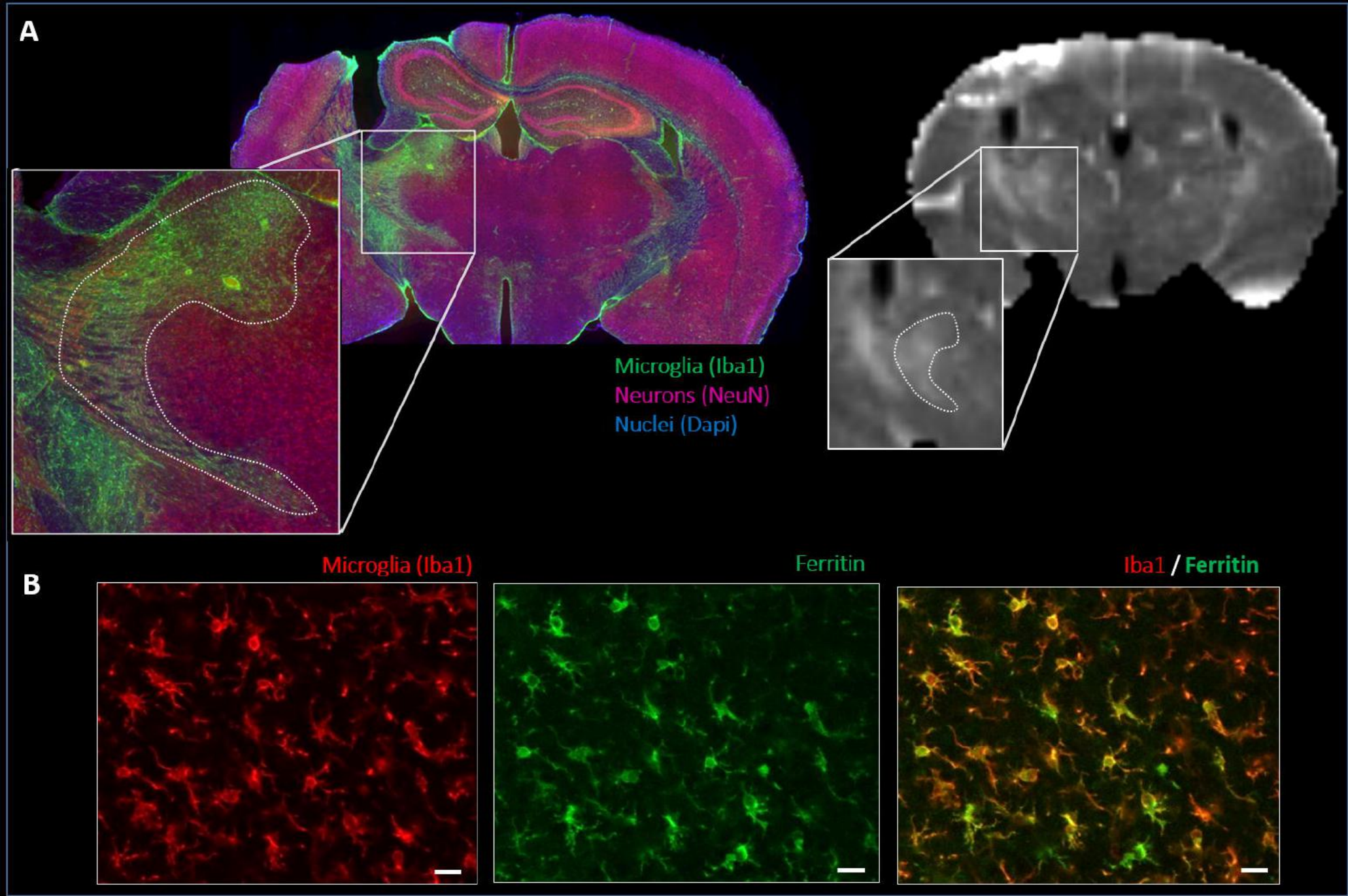
A
Microglia (Iba1)
Neurons (NeuN)
Nuclei (Dapi)
B
Microglia (Iba1)
Ferritin
Iba1 / Ferritin

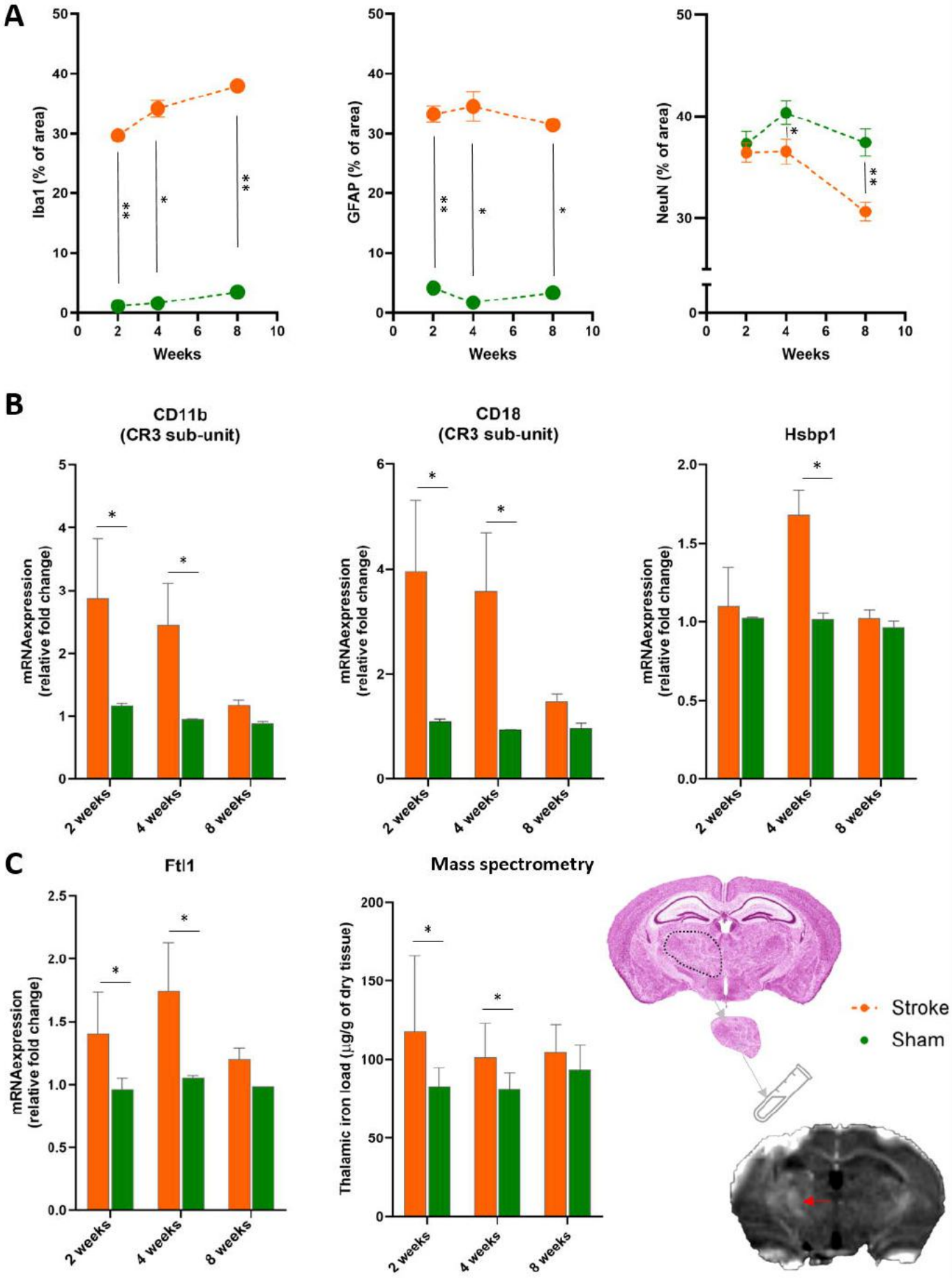
A
Iba1 (% of area)
GFAP (% of area)
NeuN (% of area)
Weeks
B
CD11b
(CR3 sub-unit)
CD18
(CR3 sub-unit)
Hsbp1
mRNAexpression
(relative fold change)
2 weeks
4 weeks
8 weeks
C
Ftl1
Mass spectrometry
Thalamic iron load (µg/g of dry tissue)
Stroke
Sham

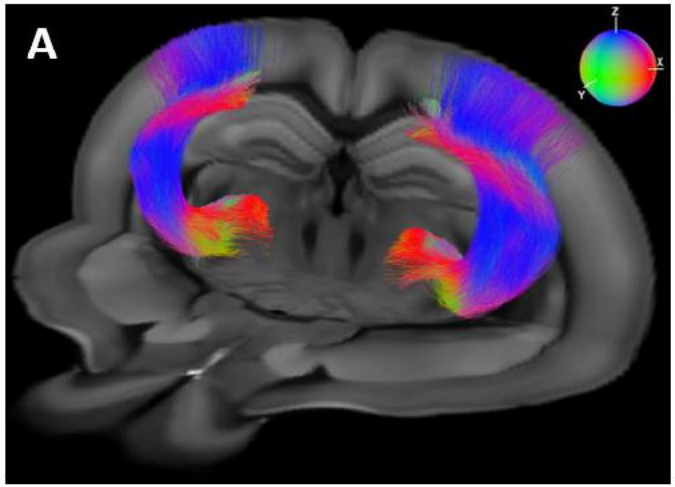
A

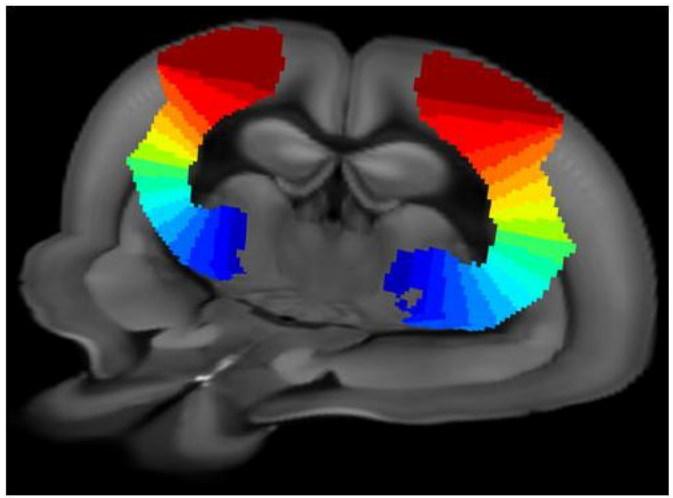

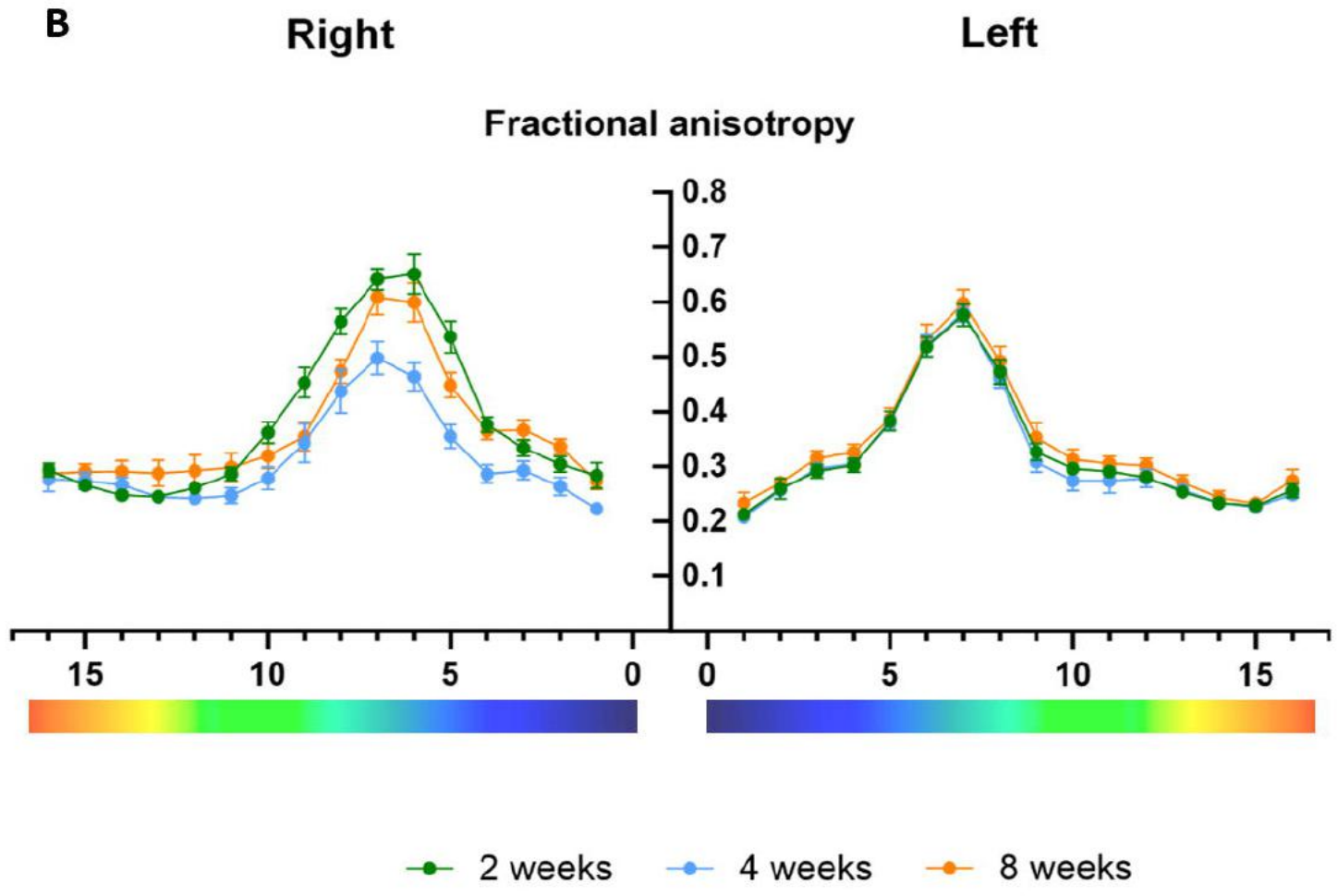
B
Right
Left
Fractional anisotropy
0.8
0.7
0.6
0.5
0.4
0.3
0.2
0.1
15
10
5
0
0
5
10
15
2 weeks
4 weeks
8 weeks

MRI R2* captures inflammation in disconnected brain structures after stroke: a translational study

Supplemental materials and methods

Study population

Participants were prospectively recruited as part of a cohort study called BBS for "Brain Before Stroke". The primary objective of this cohort was to investigate the impact of the modifications outside the infarct itself on stroke outcomes, such as those related to small vessel disease. Analysis of this objective has been reported by Coutureau *et al*. (1). We have already used this cohort to demonstrate the presence of increase R2* outside the infarct region (2, 3). The present paper is a follow-up analysis aimed at examining the relationship between disconnection patterns and delayed R2* increases, which has not previously been explored. Additionally, this cohort has been utilized in prior lesion-symptom mapping studies (4, 5), though those analyses are unrelated to the present work.

The imaging protocol included diffusion weighted images (DWI), 3D-T1-weighted images, and 2D-T2* multi echo fast gradient echo images with the following parameters:

- For DWI: 38 slices; repetition time, 9000 ms; echo time, 76 ms; slice thickness, 4 mm; matrix, 128 x 128; field of view, 240mm x 240 mm; b values, 0 and 1000 s/mm^2.
- For the 3D T1 inversion-recovery-prepared fast spoiled gradient echo sequence: 196 sagittal slices; repetition time, 8.60 ms; echo time, 3.27 ms; inversion time, 450 ms; flip angle, 12°; slice thickness, 1 mm; matrix, 256 x 256; field of view, 240mm x 240 mm.
- For the 2D multiecho fast gradient-echo sequence: 28 slices; repetition time, 775 ms; eight echo times at 4.3, 8.7, 13.0, 17.4, 21.7, 26.1, 30.5 and 34.8 ms; flip angle, 20°; slice thickness, 4 mm; matrix, 320 x 320; field of view, 240mm x 240 mm.

Out of 428 recruited patients, 156 were included for analyses focusing on the thalamus, and 177 were included for analyses focusing on the substantia nigra, according to the flowchart in **Supp-Figure-1**.

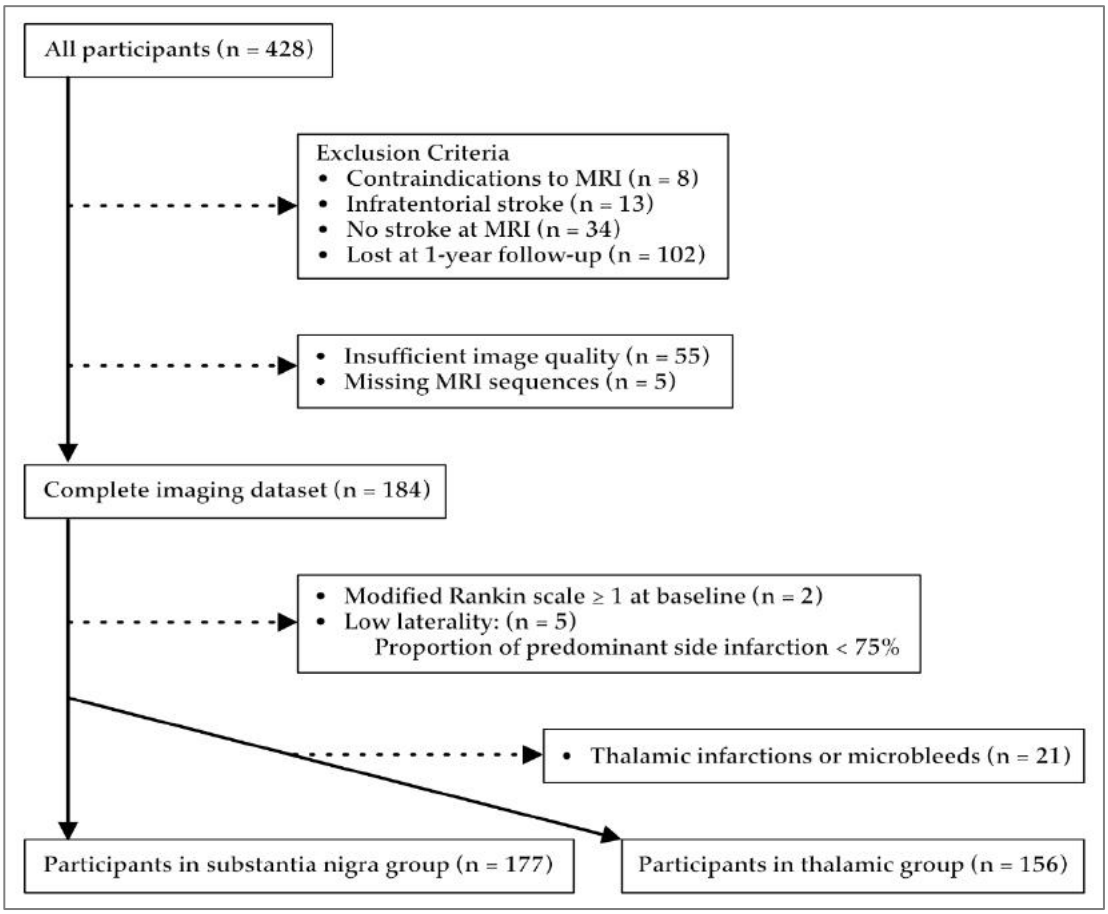

Supp-Figure 1: Flowchart of patient inclusion and exclusion

Image analyses in patients

To define the disconnection status of remote areas, we assessed the overlap between binarized disconnectivity maps and masks of thalamic nuclei groups (6) (**Supp-Figure-2, upper panel**) and substantia nigra (7) (**Supp-Figure-2, lower panel**), all available in MNI-152 space.

The disconnectivity maps represent the fibers likely to be disconnected in a given stroke patient, based on the premise that more than half of the 163 healthy participants from the Human Connectome Project (8) would exhibit fiber disconnection by an infarct in the same location (9). Therefore, the maps provide a voxel-by-voxel probability of disconnection, ranging from 0.5 to 1, excluding values below 0.5.

For thalamic nuclei, we utilized an atlas that we constructed from 7 Tesla MR images (6) taking advantage of an optimized sequence, called white matter nulled MPRAGE and providing highly contrasted images, to manually delineate thalamic nuclei (10). We combined the thalamic nuclei into 4 main groups following the definitions from Morel atlas (11) as follow:

- Anterior group: anteroventral (AV)
- Lateral group: ventral posterolateral (VPL), ventral lateral anterior (VLa), ventral lateral posterior (VLp), and ventral anterior (VA)
- Medial group: mediodorsal (MD), centromedian (CM), and habenula (Hb) (part of the epithalamus but comprised in the paraventricular complex and located at the infero-postero-medial part of the medial group and so very close to the 3rd ventricle)
- Posterior group: pulvinar (Pul), medial geniculate nucleus (MGN), and lateral geniculate nucleus (LGN)

For the substantia nigra, we used a probabilistic atlas coregistered to MNI-152 and freely available (7).

Supp-Figure 2: Schematic shows the pipeline to estimate the disconnectivity status

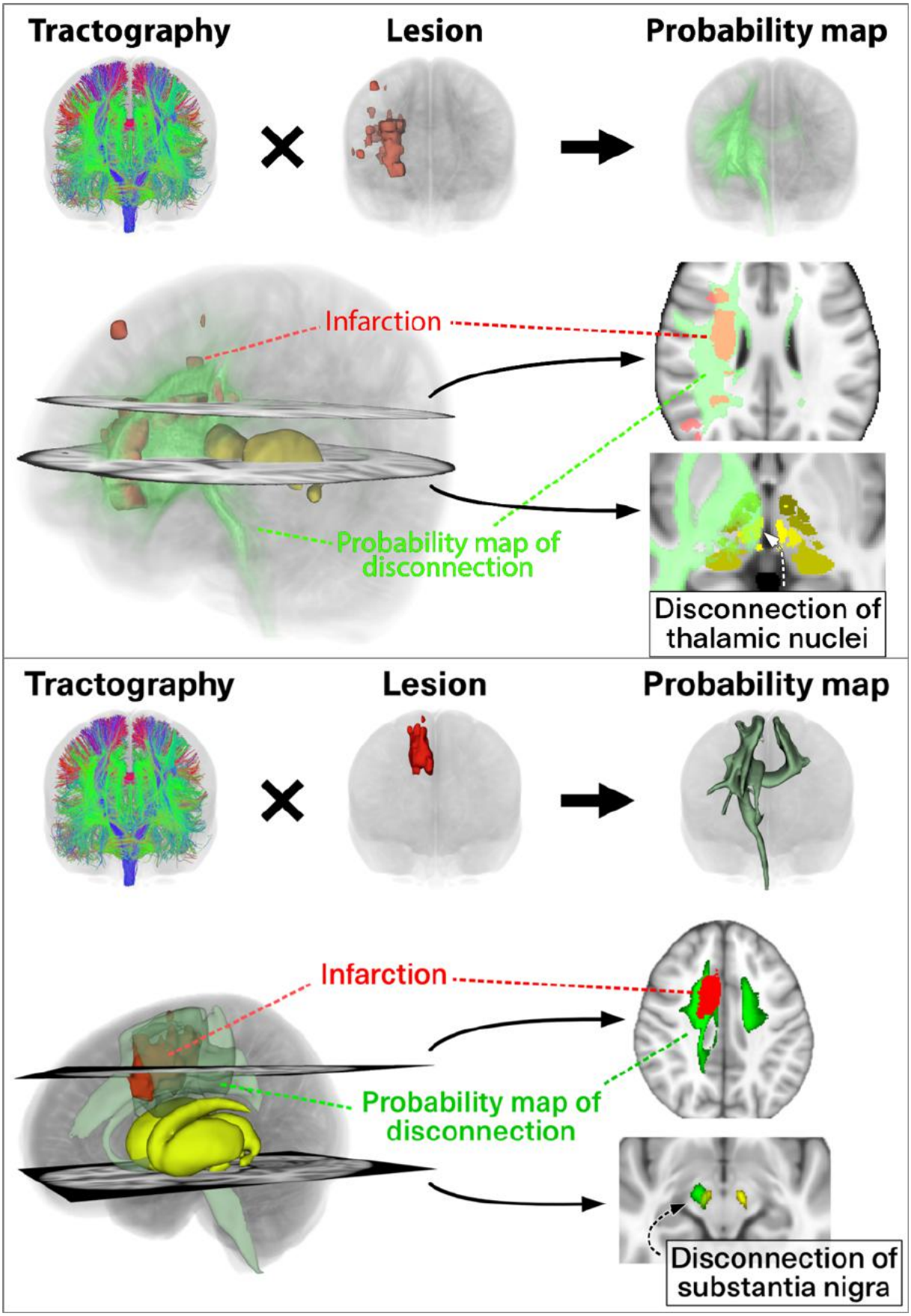

We calculated the percentage of overlap volume between the disconnectivity maps and the regions of interest ROI, which include the four thalamic groups and the substantia nigra, as follows:

$$Overlap\ (\%) = \frac{\text{Volume of overlap (diconnectivity } \subset \text{ ROI) x probablity of disconnection}}{\text{Volume ROI}} X\ 100$$

The overlap histograms for the thalamic nuclei and substantia nigra displayed a left skewed distribution, in which overlap of less than 2.5% categorized the region as "not disconnected. The distribution of the remaining percentage of overlap allowed to dichotomize "mildly disconnected" or "severely disconnected" cases using the median as a cutoff. **Supp-Figure-3** illustrates the distribution of overlap within the medial thalamic group. Similar analyses were conducted for the overlap with the lateral and posterior thalamic groups as well as with the substantia nigra. The anterior thalamic group was too small for accurate disconnection estimation using this methodology and was therefore excluded from further analysis.

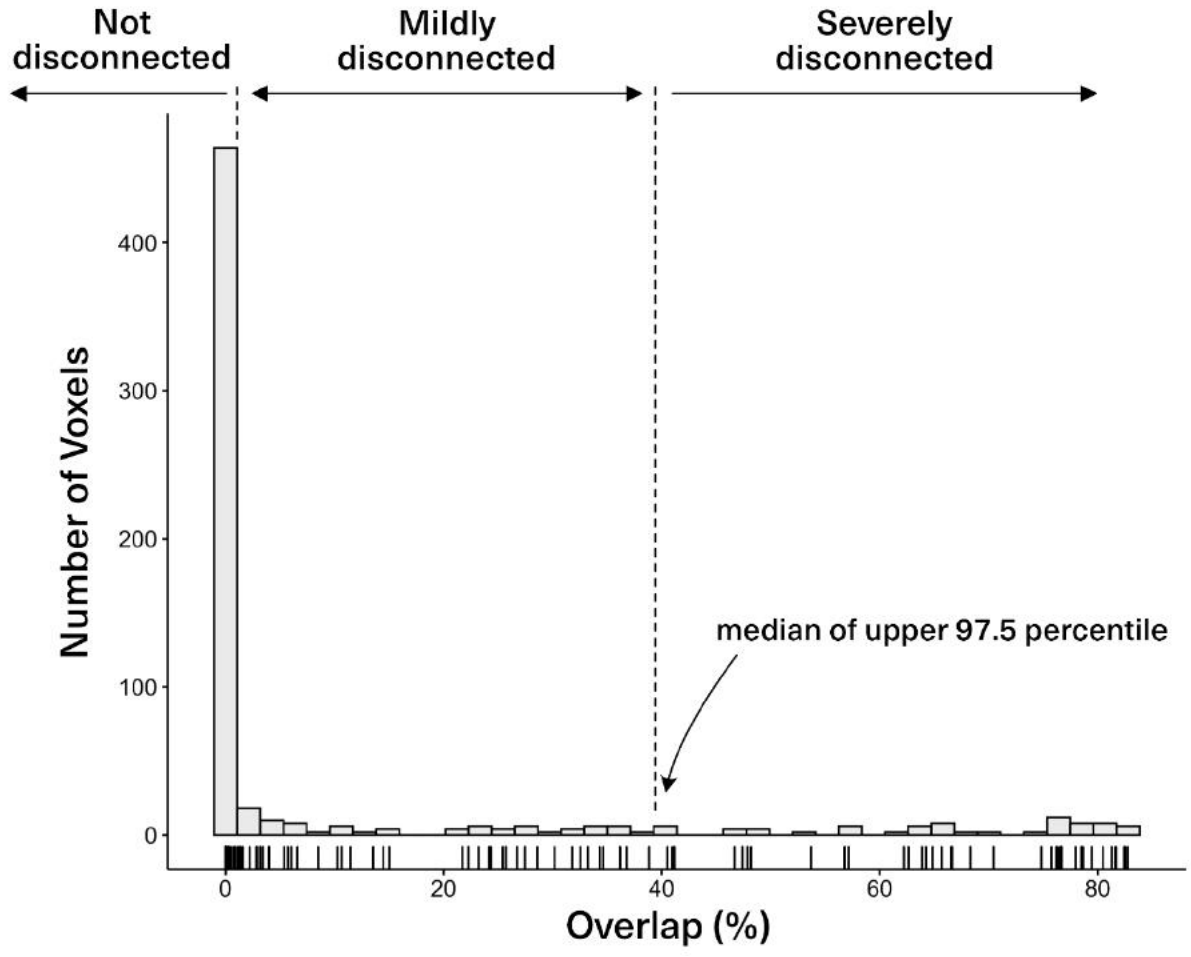

Supp-figure 3: Histogram of voxel overlap between the disconnected fibers and the medial thalamic nuclei group among the entire population, and identification of the threshold to consider the nucleus as “not disconnected”, “mildly disconnected” and “severely disconnected”.

Animal model

Mice were anesthetized using 4% isoflurane in 20% oxygen, and anesthesia was maintained at 2% isoflurane in 20% oxygen throughout the procedure. After shaving their heads, the mice were positioned in a stereotaxic frame with lidocaine-coated ear bars to minimize movement during surgery. Body temperature was maintained at 37°C using a heated blanket, and eye protection was provided with a gel (Ocry-gel, TVM, Lempdes, France) to prevent drying.

A small incision was made in the scalp to visualize the bregma and lambda, allowing precise positioning of the light source (Schott KL 1600 LED, 680 lumen, green filter, 150 Watts, 5-mm light aperture) at 0 mm antero-posterior and 2.2 mm lateral to the bregma. Rose bengal (Aldrich Chemical Company, Milwaukee, USA) was administered intraperitoneally at a dose of 10 µL/g body weight, with a concentration of 5 mg/mL in saline solution at room temperature. After a 5-minute delay, the light was turned on and directed onto the cranial bone for 10 minutes. Upon completion, the scalp was irrigated and sutured, anesthesia was gradually withdrawn, and the mice were placed in a heated recovery box. Sham procedures were identical, except for the omission of light exposure.

Animals were divided into three groups as detailed in **Supp-Figure-4**

In vivo MRI acquisition and image analyses in animals

MRI images were acquired on a 7 Tesla Bruker Biospec system (Ettlingen, Germany) equipped with a gradient system capable of 660 mT/m maximum strength and 110µs rise time. A volume resonator (75.4 mm inner diameter, active length 70 mm) operating in quadrature mode was used for excitation and a 4-element (2 × 2) phased array surface coil (outer dimensions of one coil element: 12 × 16 mm^2, total outer dimensions: 26 × 21 mm^2) was used for signal reception.

First, a 2D diffusion sequence was acquired with the following parameters: 82 slices; repetition time, 3000 ms; echo time, 24 ms; slice thickness, 500 µm; matrix, 128 x 80; field of view, 25 mm x 16 mm; b values, 0 and 1000 s/mm^2; 6 directions; 4 segments; total acquisition time, 5 min 36 s.

Supplemental material

A 3D-TrueFISP composite sequence was acquired in 8 separate sequences only differing by their RF phase advance (0°, 45°, 90°, 135°, 180°, 225°, 270° and 315°). Other parameters were the same and as follows: 112 slices; repetition time, 6 ms; echo time, 3 ms; flip angle, 27.5°; slice thickness, 145 µm; matrix, 112 x 112; field of view, 16.2 mm x 16.2 mm; total acquisition time = 12 min 15 s.

To allow R2* quantification, a 3D Multi-Echo T2*-weighted sequence was acquired with the following parameters: 112 slices; repetition time, 64.4 ms; 16 echo times with first echo, 1.61 ms; last echo, 46.61 ms and with a delta-TE of 3 ms; flip angle, 15°; slice thickness, 145 µm; matrix, 112 x 112; field of view, 16.2 mm x 16.2 mm; three averages, total acquisition time = 40 min 23 s.

We extracted R2* related metrics in specific thalamic nuclei and their volumes. For that purpose, we first applied motion correction to the multi-echo T2* images to minimize the influence of movement during image acquisition. Then, the first volume of the multi-echo images was registered to the 3D-TrueFISP using ANTs (12). The anatomical 3D-TrueFISP images were subsequently registered to the template space of a detailed mouse thalamic atlas (13) using Elastix, a robust image registration toolbox (14).

R2* maps were generated from voxel-by-voxel mono-exponential fitting of the motion-corrected and registered multi-echo T2* images and we quantified the 95th percentile of the asymmetry index (AI_{95}) in specific nuclei similarly to what we did in patients.

Next, an inverse transformation was applied to project back the thalamic nuclei regions from the atlas space into the native 3D-TrueFISP space. Finally, volumes of the specific nuclei were calculated using the segmented regions obtained from the inverse transformation, and were expressed as asymmetry index (AI) compared to the volumes of contralateral nuclei.

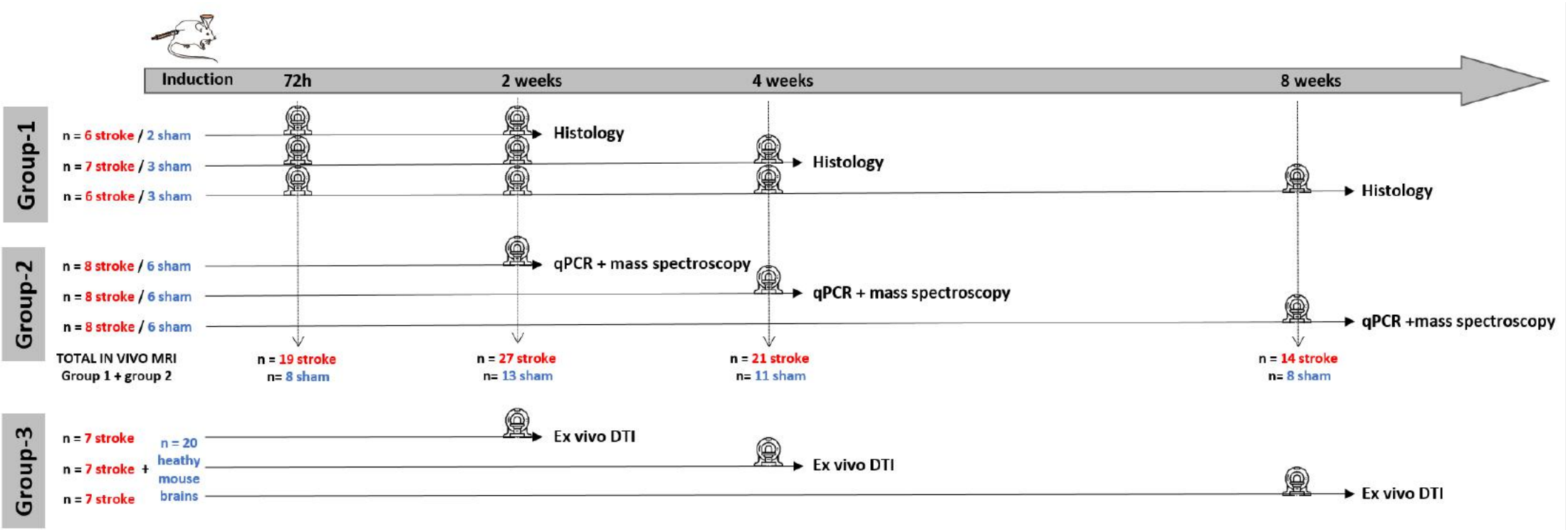

Supp-Figure 4: Experimental design indicating the different groups. The pictograms along the timeline indicate magnetic resonance imaging sessions, either *in vivo* for the groups 1 and 2, or *ex vivo* for the group 3.

Biological analyses

Immunohistochemistry

Mice from the group-1 used for histological analyses were deeply anesthetized with Exagon and lidocaine and perfused transcardially with saline followed by PBS solution containing 4% paraformaldehyde solution, for 8 min. The brains were then removed and transferred into a 4% paraformaldehyde solution, for post-fixation. They were then transferred into a Tris-buffered saline (TBS) containing 30% sucrose and 0.05% sodium azide, to allow cryoprotection, frozen in OCT (Tissue-Tek®, Sakura Finetech, USA) and stored at -80°C until use. A tissue block containing the thalamus was then cut into 30 µm thick coronal sections with a cryostat (Leica CM 1950, Nussloch, Germany).

Immunostaining was performed for microglia (anti-Iba1), astrocytes (anti-GFAP), neurons (anti-NeuN) and ferritin (anti-ferritin) using single and double (Iba1+ferritin, Iba1 + NeuN) staining. Free-floating sections were rinsed in TBS and incubated overnight in a TBS solution containing 0.25% Triton X-100, 1% normal donkey serum and diluted primary antiserum. The following antisera were used: goat anti-Iba1 (1:2000; ABCAM, Ab5076), rabbit anti-Iba1 (1:1000; Sobioda, W1W019-19741), rabbit anti-GFAP (1:2000; DAKO, Z0334), chicken anti-NeuN (1:1500; MERCK, ABN91) and rabbit anti-ferritin light chain (1:800; ABCAM, Ab69090). Afterwards, sections were washed in TBS and incubated using the secondary antibodies (donkey IgGs): anti-rabbit Alexa Fluor 488 (1/1000; Jackson, 711-545-152), anti-goat TRITC (1/1000; Jackson, 705-025-147), anti-rabbit TRITC (1/1000; Jackson, 711-025-152) or anti-chicken TRITC (1/1000; Jackson, 703-025-155) in a TBS solution containing 0.25% Triton X100 (2 h at room temperature). A mounting medium containing DAPI was used for coverslipping (Vectashield H-1200).

Sections were imaged for quantitative analyses on NanoZoomer wide field microscope (Hamamatsu nanozoomer 2.0HT) equipped with a 40x objective and a CCD camera. This system was driven by Mercator software and used to scan slides (mosaic images) for direct comparison with MRI. Identical laser intensity and exposure settings were applied to all tissue sections. At least 2 tissue sections containing the thalamus were randomly selected and quantitative results were averaged. Images were analyzed using ImageJ software. Regions of interest (ROI) outlining thalamic VPL and VPM nuclei were manually drawn using atlas to guide the delineation. Staining areas were quantified automatically as percent of immunoreactivity after subtracting background and thresholding identically all the images for conversion to binary masks.

Laser capture microdissection

The mice from group-2 were deeply anesthetized with Exagon and lidocaine and perfused transcardially with PBS for 1 min 30 s. Their brains were quickly extracted, flash-frozen in a vial of isopentane that was immersed in dry ice and subsequently stored at -80 °C until sectioning. Brains were cut using 50 µm thick coronal sections on a freezing microtome (CM3050 S Leica) at -22 °C to prevent RNA degradation. Tissue sections were mounted on PENmembrane 1 mm glass slides (P.A.L.M. Microlaser Technologies AG, Bernried, Germany) that had been pretreated to inactivate RNase. Frozen sections were fixed in a series of precooled ethanol baths (40 s in 95%, 75% and 30 s in 50%) and stained with cresyl violet 1% for 20 s. Subsequently, sections were dehydrated in a series of precooled ethanol baths (30 s in 50%, 75% and 40 s in 95% and in anhydrous 100% twice). Immediately after dehydration laser capture microdissection was performed with a P.A.L.M MicroBeam microdissection system version 4.0-1206 equipped with a P.A.L.M. RoboSoftware (P.A.L.M. Microlaser Technologies AG, Bernried, Germany). Laser power and duration were adjusted to optimize capture efficiency. Microdissection was performed at 5x magnification. The whole thalamus was captured to maximize the amount of material and because isolation of specific nuclei was very difficult to conduct in such conditions. The material was split in 2 adhesive caps (P.AL.M Microlaser Technologies AG, Bernried, Germany) with a 1 slice for qPCR every 3 slices for mass spectrometry.

Quantitative real-time PCR (qPCR)

For RNA analysis, we added 150 µl of extraction buffer provided in a ReliaPrep™ RNA Cell Miniprep System (Promega) to the caps and stored at -80 °C until RNA isolation. Total RNA was extracted from microdissected tissues by using the ReliaPrep™ RNA Cell Miniprep System (Promega, Madison, USA) according to the manufacturer's protocol. The concentration of RNA was determined with Nanodrop 1000. RNA qualities were performed using Agilent RNA 6000 Pico Kit on 2100 Bioanalyzer (Agilent Technologies, Santa Clara, CA).

RNA was processed and analyzed according to an adaptation of published methods (15). Briefly, cDNA was synthesized from 90 ng of total RNA by by using Maxima Reverse Transcriptase (Thermo Scientific). qPCR was performed with a LightCycler® 480 Real-Time PCR System (Roche, Meylan, France). qPCR reactions were done in duplicate for each sample by using transcript-specific primers, cDNA (2.6 ng) and LightCycler 480 SYBR Green I Master (Roche) in a final volume of 10 µl. The qPCR data were exported and analyzed in an informatics tool (Gene Expression Analysis Software Environment) developed at our institute. For the determination of the reference genes, the RefFinder method was used (16). Relative expression analysis was normalized against two reference genes. In particular,

peptidylprolyl isomerase A (Ppia) and non-POU-domain-containing, octamer binding protein (Nono) were used as reference genes here. To estimate the PCR amplification efficiency, standard curves were determined, and all the primers chosen were 100% efficient. The relative level of expression was calculated with the comparative ($2^{-\Delta\Delta CT}$) method (17). The following primer sequences were used

Table X. Primer Sequences.

Gene	**GenBank ID**	**Forward Sequence (5'-3')**	**Reverse Sequence (5'-3')**
Itgb2 (CD18)	NM_008404	TCGGTTTCTTTCCGCCATTA	AAGATTGTGCAGGTCGGAAGAC
Itgam (CD11b)	NM_001082960	CTCATCACTGCTGGCCTATACAA	GCAGCTTCATTCATCATGTCCTT
Hsbp1	U03560	ACGAAGAAAGGCAGGACGAA	ACCTGGAGGGAGCGTGTATTT
Nono	NM_023144	CTGTCTGGTGCATTCCTGAACTAT	AGCTCTGAGTTCATTTTCCCATG
Ppia	NM_008907	CAAATGCTGGACCAAACACAA	GCCATCCAGCCATTCAGTCT
Ftl1	NM_010240	GGACCCTCATCTCTGTGACTTCC	GCCCATCTTCTTGATGAGTTTCA

Mass spectrometry

For chemically iron concentration, we used inductively coupled mass spectrometry.

All samples were handled with care in order to avoid environmental contamination during their manipulation.

Brain tissue samples, stored at -80°C, were desiccated at 120°C for 15 hours in an oven. Then, dried samples were weighed and mineralized by nitric acid solution in Teflon PFA-lined digestion vessels. Acid digestion was carried out at 180°C using ultrapure concentrated HNO3 (69%) (Fisher Chemical Optima Grade) in microwave oven device (Mars 6, CEM®).

Iron was measured by Inductively Coupled Plasma Mass Spectrometry (ICP-MS), on an ICAP-TQ from Thermo Scientific® equipped with collision cell technology. The source of plasma was argon (Messer®) with high degree of purity (>99.999%). The collision/reaction cell used was pressurized with helium (Messer®). All rinse, diluent, and standards were prepared with ≥18 MΩ cm ultrapure water using a Millipore® MilliQ Advantage A10 water station.

Digested samples were diluted 1:20 by addition of a diluent solution consisting of 0.5% (v/v) HNO_3 (Optima Grade Fischer Chemical®). The internal standard used was rhodium (Fisher Scientific®). Calibration ranges preparation was carried out using a multi-element calibrator solution (SCP Science® Plasma Cal). Calibration and verification of instrument performance were realized using multi-element solutions (Thermo®). Quality control was Clincheck controls for trace elements (Recipe). The accuracy of the ICP-MS assay method was verified through analysis of certified reference materials (NCS ZC71001) and participation in External Quality Assessment Schemes (EQAS) organized by OELM (Occupational and Environmental Laboratory Medicine).

Ex vivo Image acquisition and analyses in animals

Two groups of ex vivo mouse brains were used:

- 20 healthy mice to build a bilateral template of a thalamo-cortical tract connecting the infarct region to the specific altered thalamic nuclei;

- 21 stroke mice to explore the white matter microarchitecture changes along this thalamo-cortical tract at 2-, 4-, and 8-weeks post-stroke (n=7 per group).

Healthy animal preparation and diffusion MRI acquisition

The healthy mice were deeply anesthetized at 8 weeks and perfused transcardially with saline followed by PBS solution containing 4% paraformaldehyde solution. Brains were extracted, postfixed in 4% paraformaldehyde overnight and placed on a custom 3D-printed apparatus to prevent movement during the MR acquisition. Each brain in a 3D-printed apparatus was then put into a transparent falcon (1.5mL) and immersed for two days in a proton-free solution of Fomblin YVAC L 14/6 (Kurt J. Lesker) before imaging.

Images were acquired using the 7T Bruker Biospec 70/20 system (Ettlingen, Germany) scanner with a standard Bruker cross coil setup with a quadrature surface coil for mice. Diffusion imaging was acquired using a 3D diffusion-weighted Spin-Echo EPI sequence with the following parameters: 82 slices; repetition time, 1000 msec; echo time, 30 msec; slice thickness, 121µm; matrix, 170 x 110; field of view, 18 mm x 13 mm resulting in a native image resolution of 105 x 118 x 121 μm^3; b-values, 0 and 1500 s/mm^2; 60 unique diffusion directions and five non-diffusion direction (b0) measurements; total acquisition time, 9 hours.

Diffusion MRI data processing

Diffusion-weighted data pre-processing and analysis were performed with a combination of tools, namely FSL (18), MRtrix3 (19), ANTs (12), and DIPY-based SCILPY (20) (github.com/scilus/scilpy). First, raw MRI files were converted to the standard NifTi format and compressed. Next, preprocessing steps were carried out: b0 images were extracted, averaged, and used to create a mask of the whole brain; homogeneity and eddy current corrections were carried out. The averaged b0 volume was aligned to the Allen Mouse Brain Atlas (AMBA) (21) at the 70 µm isotropic resolution using ANTs. Both linear and nonlinear matrices were then used to align the native DWI data in the AMBA space. The fractional anisotropy (FA) maps were then computed.

Tractography was carried out using a constrained spherical deconvolution local tracking algorithm (22) with the following parameter (theta = 20°, step size = 0.05 mm, min/max length 2/20 mm, number of seeds/voxels = 500 in the seeding mask). The seeding mask corresponded to the concatenated white matter ROIs of the AMBA, while the tracking mask was the whole brain mask computed from the averaged b0 volume.

Extracting a thalamo-cortical tract and building a bilateral template

Each whole brain tractogram was filtered to extract the streamlines connecting the infarct region to the specific thalamic nuclei in the right hemisphere. First, the cortical infarct regions induced *via* photothrombotic ischemia (n=12 out of the 21 stroke mice) were manually delineated and aligned with the AMBA space, resulting in a single averaged fronto-parietal infarct region. Second, the right thalamic nuclei in AMBA, specifically the ventral posterolateral (VPL) and ventral posteromedial (VPM) nuclei, regions affected by the induced stroke, were selected as the second filtering ROI. We concatenated the 20 thalamo-cortical tracts to create the right hemisphere's final template (Figure 6A, top). Given the symmetrical structure of the AMBA, this right-hemisphere template was mirrored across the interhemispheric plane to generate a corresponding template for the left hemisphere.

Fractional anisotropy measurements

We used a tract profile approach to estimate the FA values along the thalamo-cortical template in the stroke mice at 2-, 4-, and 8-weeks post-stroke (7 mice per time point). The label image of the thalamo-cortical template represented the coverage of the segmented tract into regions labeled from 1 to 20, starting from the thalamic nuclei (Figure 6A, bottom). We then calculated the mean (± standard deviation) FA values within each labeled region for each stroke mouse at each post-stroke duration (Figure 6B).

Supplemental results

Supplemental results on substantia nigra disconnection in patients

Supp-Table 1 shows the characteristics of the patients included in the substantia nigra analysis.

Variables	Participants included in the substantia nigra analysis (n=177)
Demographics	
Age (y)*	65 (56, 77)
Sex	
M	120 (68)
F	57 (32)
Hypertension	112 (63)
Diabetes mellitus	28 (16)
Active smoking	83 (47)
Body mass index (Kg/m²)*	26.7 (24.2, 29.3)
Baseline visit	
NIHSS score*	3.0 (2.0, 6.0)
Time from onset to baseline MRI (h)*	47 (33, 60)
Recanalization procedure (thrombolysis and/or thrombectomy)	85 (48)
Infarct volume (mL)*	10 (2, 29)
Follow-up visit	
Time from onset to follow-up (y)*	1.0 (0.98, 1.01)
NIHSS score*	0.5 (0.0, 2.0)
Modified Rankin scale (mRS)*	1.0 (0.0, 2.0)

Except where indicated, data are numbers of patients with percentages in parentheses. * Data are median, with IQRs in parentheses..

Supp-Table 2: characteristics of the population according to the disconnectivity status for the lateral, medial and posterior thalamic nuclei groups and for the substantia nigra.

	Lateral group of thalamic nuclei			Medial group of thalamic nuclei			Posterior group of thalamic nuclei			Substantia nigra		
	Not disconnected	Mildly disconnected	Severely disconnected	Not disconnected	Mildly disconnected	Severely disconnected	Not disconnected	Mildly disconnected	Severely disconnected	Not disconnected	Mildly disconnected	Severely disconnected
	n=50	n=53	n=53	n=79	n=38	n=39	n=60	n=48	n=48	n=54	n=61	n=62
Age (y)*	67 (57 – 77)	63 (54 – 71)	66 (60 – 77)	66 (57 – 77)	62 (51 – 76)	66 (60 – 75)	66 (56 – 78)	63 (57 – 74)	65 (57 – 74)	68 (56 – 77)	63 (55 – 73)	66 (58 – 76)
M / F	38 (76) / 12 (24)	40 (75) / 13 (25)	30 (57) / 23 (43)	60 (76) / 19 (24)	25 (66) / 13 (34)	23 (59) / 16 (41)	45 (75) / 15 (25)	35 (73) / 13 (27)	28 (58) / 20 (42)	42 (78) / 12 (22)	41 (67) / 20 (33)	37 (60) / 25 (40)
Hypertension	26 (52)	36 (68)	39 (74)	51 (65)	23 (61)	27 (69)	32 (53)	33 (69)	36 (75)	30 (56)	41 (67)	41 (66)
Diabetes mellitus	5 (10)	11 (21)	10 (19)	12 (15)	9 (24)	5 (13)	8 (13)	9 (19)	9 (19)	5 (9.3)	12 (20)	11 (18)
Active smoking	21 (42)	28 (53)	23 (43)	35 (44)	21 (55)	16 (41)	28 (47)	22 (46)	22 (46)	25 (46)	30 (49)	28 (45)
Body mass index (Kg/m^2)*	26.8 (24.3 – 29.6)	25.9 (24.0 – 28.3)	27.7 (24.1 – 30.1)	26.5 (24.2 – 29.0)	26.1 (23.7 – 28.4)	27.7 (25.4 – 30.1)	25.6 (23.8 – 28.4)	26.5 (23.8 – 28.4)	28.3 (26.2 – 30.4)	26.8 (24.4 – 29.7)	25.7 (23.9 – 27.8)	27.7 (24.2 – 30.2)
Baseline NIHSS score*	2 (1 – 3)	3 (2 – 4)	7 (4 – 13)	2 (1 – 3)	4 (3 – 7)	6 (3 – 16.5)	2 (1 – 3)	3 (2 – 5)	7 (4 – 13)	2 (1 – 2)	3 (2 – 5)	6 (3 – 13)
Baseline Infarct volume (mL)*	7.90 (1.50 – 16.49)	3.90 (0.89 – 15.85)	19.49 (8.31 – 65.92)	5.89 (1.23 – 13.74)	4.93 (1.75 – 21.43)	27.05 (15.32 – 80.58)	5.60 (1.31 – 13.02)	9.03 (1.70 – 21.23)	22.96 (5.85 – 70.96)	7.90 (1.50 – 17.01)	2.40 (0.90 – 11.68)	20.38 (8.75 – 52.34)
NIHSS score at follow-up*	0 (0 – 1)	0 (0 – 1)	2 (1 – 6)	0 (0 – 1)	1 (0 – 3)	1 (0.5 – 6)	0 (0 – 1)	1 (0 – 1)	2 (0 – 6)	0 (0 – 1)	1 (0 – 2)	1 (0 – 5)
mRS at follow-up*	0 (0 – 1)	1 (0 – 1.25)	2 (1 – 3)	0 (0 – 1)	2 (1 – 2)	1.5 (1 – 3)	0.5 (0 – 1)	1 (0 – 2)	2 (1 – 3)	0 (0 – 1)	1 (0.5 – 2)	2 (0.25 – 3)

Except where indicated, data are numbers of patients with percentages in parentheses. * Data are median, with IQRs in parentheses.

Participants with severely disconnected substantia nigra showed a significant increase of AI_{95} from baseline to 1 year while there was no modification of AI_{95} if this structure was not or mildly disconnected (**Supp-Figure-5**).

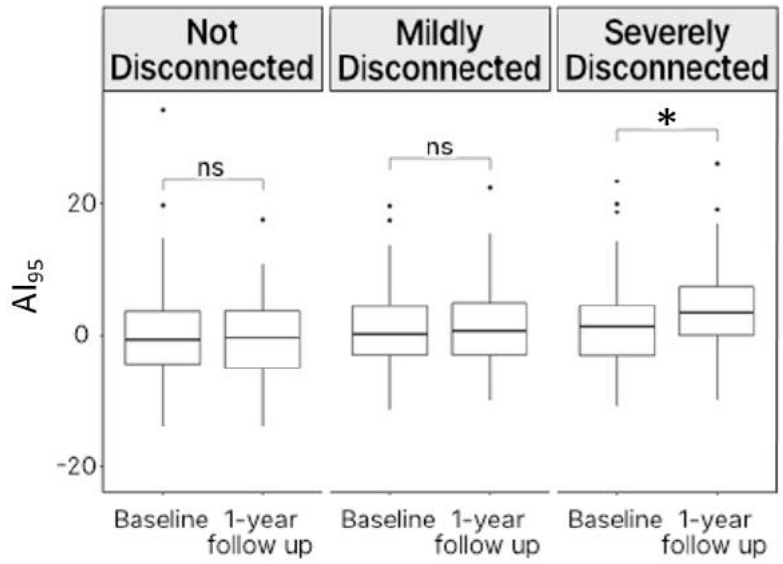

Supp-Figure 5 shows the relationship between the substantia nigra disconnectivity status and the secondary R2* increase at 1-year follow-up.

The linear regression confirmed that the disconnectivity status of susbtantia nigra at baseline was a significant and independent predictor of AI_{95} at follow-up (**Supp-Table 3**).

Supp-Table 3: Multivariable linear regression models for prediction of AI_{95} at 1 year in substantia nigra

Variable	B value (95%CI	*P* Value
Disconnection of the SUBSTANTIA NIGRA		
Age (+1 y)	-0.03 (-0.18, 0.11)	0.70
Sex (F)	-0.15 (-0.40, 0.17)	0.40
AI_{95} at baseline (+ 1)	**0.15 (0.01, 0.30)**	**0.042***
Infarct volume (+ 1 mL)	0.12 (-0.04, 0.27)	0.13
Disconnection		

Mildly disconnected	0.26 (-0.10, 0.62)	0.20
Severely disconnected	**0.55 (0.18, 0.92)**	**0.004****

Supplemental results on the photothrombosis stroke model in mice

The photothrombosis model induced a reproducible lesion within the sensory motor cortex **(Supp-Figure-6)**

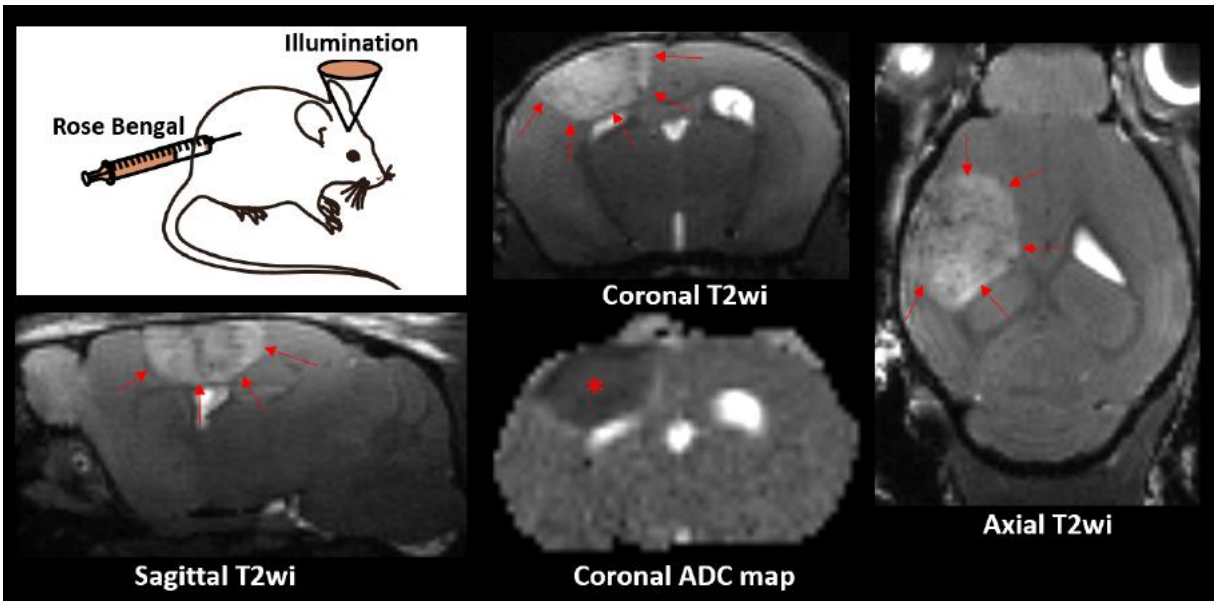

Supp-Figure 6 shows a schematic representation of the photothrombosis model that consists in transcranial illumination of the brain 5 minutes after intraperitoneal injection of the Rose Bengal photosensitive dye. After a delay of 72h, we verified with MRI that we consistently induced a focal cortical stroke (delineated by arrows on T2 weighted images) that showed low ADC values (*) in line with the cytotoxic edema encountered at the acute stage on an infarct.

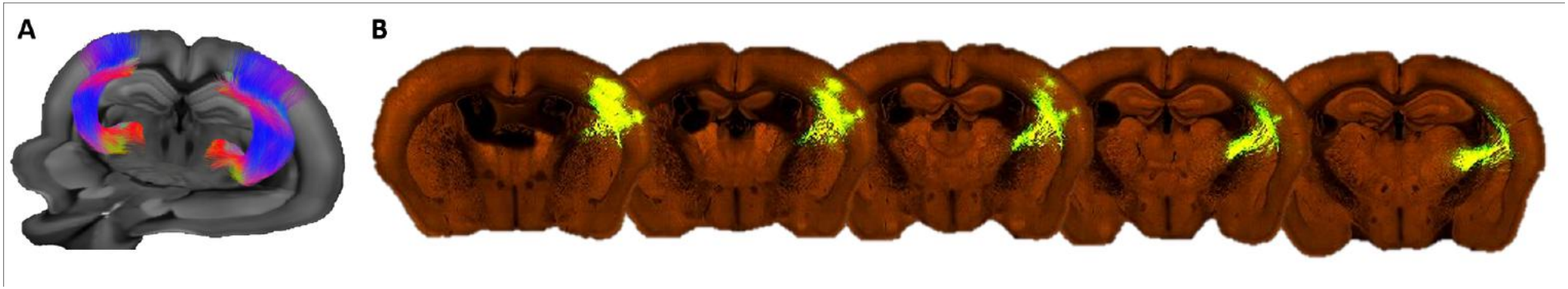

Supp-Figure 7: (A) shows the 3D projection of fibers connecting the cortical site to ipilateral VPL and VPM from diffusion tensor MRI. **(B)** shows the close correspondence with serial two-photon tomography after 0.18 mm^3 EGFP tracer injected in VPL and VPM of Slc17a6-IRES-Cre mice from mouse connectivity data from the Allen Brain Atlas portal (23).

Supplemental references

1. Coutureau J, Asselineau J, Perez P, et al. Cerebral Small Vessel Disease MRI Features Do Not Improve the Prediction of Stroke Outcome. Neurology. 2021;96(4):e527-e37.

2. Kuchcinski G, Munsch F, Lopes R, et al. Thalamic alterations remote to infarct appear as focal iron accumulation and impact clinical outcome. Brain. 2017;140(7):1932-46.

3. Linck PA, Kuchcinski G, Munsch F, et al. Neurodegeneration of the Substantia Nigra after Ipsilateral Infarct: MRI R2* Mapping and Relationship to Clinical Outcome. Radiology. 2019;291(2):438-48.

4. Munsch F, Sagnier S, Asselineau J, et al. Stroke Location Is an Independent Predictor of Cognitive Outcome. Stroke. 2016;47(1):66-73.

5. Fukutomi H, Yamamoto T, Sibon I, et al. Location-weighted versus Volume-weighted Mismatch at MRI for Response to Mechanical Thrombectomy in Acute Stroke. Radiology. 2023;306(2):e220080.

6. Saranathan M, Iglehart C, Monti M, Tourdias T, Rutt B. In vivo high-resolution structural MRI-based atlas of human thalamic nuclei. Sci Data. 2021;8(1):275.

7. Keuken MC, Forstmann BU. A probabilistic atlas of the basal ganglia using 7 T MRI. Data Brief. 2015;4:577-82.

8. Glasser MF, Smith SM, Marcus DS, et al. The Human Connectome Project's neuroimaging approach. Nat Neurosci. 2016;19(9):1175-87.

9. Foulon C, Cerliani L, Kinkingnehun S, et al. Advanced lesion symptom mapping analyses and implementation as BCBtoolkit. Gigascience. 2018;7(3):1-17.

10. Tourdias T, Saranathan M, Levesque IR, Su J, Rutt BK. Visualization of intra-thalamic nuclei with optimized white-matter-nulled MPRAGE at 7T. Neuroimage. 2014;84:534-45.

11. Morel A, Magnin M, Jeanmonod D. Multiarchitectonic and stereotactic atlas of the human thalamus. J Comp Neurol. 1997;387(4):588-630.

12. Avants BB, Tustison NJ, Song G, Cook PA, Klein A, Gee JC. A reproducible evaluation of ANTs similarity metric performance in brain image registration. Neuroimage. 2011;54(3):2033-44.

13. Hikishima K, Komaki Y, Seki F, Ohnishi Y, Okano HJ, Okano H. In vivo microscopic voxel-based morphometry with a brain template to characterize strain-specific structures in the mouse brain. Sci Rep. 2017;7(1):85.

14. Klein S, Staring M, Murphy K, Viergever MA, Pluim JP. elastix: a toolbox for intensity-based medical image registration. IEEE Trans Med Imaging. 2010;29(1):196-205.

15. Bustin SA, Benes V, Garson JA, et al. The MIQE guidelines: minimum information for publication of quantitative real-time PCR experiments. Clin Chem. 2009;55(4):611-22.

16. Xie F, Xiao P, Chen D, Xu L, Zhang B. miRDeepFinder: a miRNA analysis tool for deep sequencing of plant small RNAs. Plant Mol Biol. 2012.

17. Livak KJ, Schmittgen TD. Analysis of relative gene expression data using real-time quantitative PCR and the 2(-Delta Delta C(T)) Method. Methods. 2001;25(4):402-8.

18. Jenkinson M, Beckmann CF, Behrens TE, Woolrich MW, Smith SM. Fsl. Neuroimage. 2012;62(2):782-90.

19. Tournier JD, Smith R, Raffelt D, et al. MRtrix3: A fast, flexible and open software framework for medical image processing and visualisation. Neuroimage. 2019;202:116137.

20. Garyfallidis E, Brett M, Amirbekian B, et al. Dipy, a library for the analysis of diffusion MRI data. Front Neuroinform. 2014;8:8.

21. Wang Q, Ding SL, Li Y, et al. The Allen Mouse Brain Common Coordinate Framework: A 3D Reference Atlas. Cell. 2020;181(4):936-53 e20.

22. Descoteaux M, Deriche R, Knosche TR, Anwander A. Deterministic and probabilistic tractography based on complex fibre orientation distributions. IEEE Trans Med Imaging. 2009;28(2):269-86.

23. https://connectivity.brain-map.org/.